Universidade de Aveiro
2022

FÁBIO HENRIQUE BAPTISTA DE FREITAS

Desenvolvimento de sensores em fibra ótica para avaliação do desempenho e segurança de baterias de iões de lítio

Development of optical fiber sensors to evaluate the performance and safety of lithium-ion batteries

Universidade de Aveiro
2022

FÁBIO HENRIQUE BAPTISTA DE FREITAS

Desenvolvimento de sensores em fibra ótica para avaliação do desempenho e segurança de baterias de iões de lítio

Development of optical fiber sensors to evaluate the performance and safety of lithium-ion batteries

Dissertação apresentada à Universidade de Aveiro para cumprimento dos requisitos necessários à obtenção do grau de Mestre em Engenharia Física, realizada sob a orientação científica do Doutor Micael dos Santos Nascimento, Investigador doutorado do i3N e do Departamento de Física da Universidade de Aveiro, e do Doutor Carlos Alberto Ferreira Marques, Investigador Principal do i3N e do Departamento de Física da Universidade de Aveiro

The author gratefully acknowledges the European Project "Innovative physical/virtual sensor platform for battery cell" (INSTABAT) (European Union's Horizon 2020 research and innovation program under grant agreement No 955930), https://www.instabat.eu/.

Dedico esta dissertação ao meu avô. Espero que estejas orgulhoso de mim.

o júri

presidente

Doutora Teresa Maria Fernandes Rodrigues Cabral Monteiro
Professora Associada com Agregação do Departamento de Física da Universidade de Aveiro

vogais

Doutor José Luís Campos de Oliveira Santos
Professor catedrático da Faculdade de Ciências da Universidade do Porto

Doutor Micael dos Santos Nascimento
Investigador doutorado do i3N e do Departamento de Física da Universidade de Aveiro

agradecimentos

Desde o início de 2021 que a vida me tem colocado muitos desafios para ultrapassar… Mas, como costumo dizer, há bens que vêm por mal, e ganhei uma capacidade de resiliência brutal que me ajudou a seguir o meu caminho. Assim, o primeiro agradecimento é para mim. O segundo é para os meus pais e para a minha irmã, por estarem ao meu lado desde o primeiro dia e ajudarem-me a manter um bom espírito.

Aos meus amigos, o Zé, o Gonçalo, o "Cimento", o David e o Gata, agradeço todos os bons momentos que me proporcionaram. Quem diria que Elasticidade estaria na base da nossa amizade…

Agradeço a todos os professores que me acompanharam no meu percurso académico, em particular à investigadora Doutora Marta Ferreira, que me provocou um gosto particular por sensores de fibra ótica. Aos investigadores Doutor Micael Nascimento e Doutor Carlos Marques endereço um agradecimento especial pela confiança depositada em mim para contribuir para este projeto e por toda a paciência que tiveram comigo. Desfrutei de cada momento, mesmo quando os sensores partiam. Ao Lucca Matuck, obrigado por toda a ajuda neste projeto. Foste uma parte importante dele.

Agradeço, também, ao aluno de doutoramento Luís Fontes, do Departamento de Química, por ter disponibilizado a câmara de luvas para a perfuração das baterias e introdução dos sensores. Ao Departamento de Física e ao laboratório i3N, agradeço por disponibilizarem acesso às suas instalações e a todo o material necessário para a realização deste projeto. Agradeço ao *Leibniz-Institut für Photonische Technologien* pelo fornecimento das fibras *hollow-core* para o desenvolvimento dos sensores híbridos.

Espero que o futuro seja risonho para mim.

palavras-chave Sensor em fibra ótica, baterias de iões de lítio, pressão, temperatura, monitorização simultânea

resumo

A dependência da sociedade em combustíveis fósseis está a tornar-se num grande obstáculo no que toca à sustentabilidade ambiental. O poder político concentrado nas instituições relacionadas com o mercado de combustíveis fósseis representa uma dependência energética global. Fontes de energia alternativas podem ser exploradas para fornecer toda a energia da atividade humana e distribuí-la melhor pelo mundo. Todavia, para se utilizar estas energias alternativas, é necessário consumi-las imediatamente ou armazená-las como energia potencial, senão serão desperdiçadas. Múltiplas áreas estão a investir para procurar reduzir o uso de combustíveis fósseis ao estimular a investigação e o desenvolvimento de fontes de energia alternativas que, juntamente com o desenvolvimento de formas de armazenar energia, é crucial para potencializar a utilização e adoção de tais energias. Atualmente, baterias de iões de Lítio (LiBs) são as mais utilizadas, escaladas e pedidas fontes de armazenamento de energia pelo mundo.

A falta de informação sobre o interior das baterias atualmente dificulta o aumento da precisão e capacidade de previsão dos atuais algoritmos e modelos dos sistemas de gestão das baterias (BMS), enquanto limita as tentativas para refinar o design térmico das baterias devido à ausência de informação sobre as transferências de calor. Isto levou ao aumento do interesse nas imagens tempo-espaciais dos fluxos térmicos dentro de uma bateria através de sensores de temperatura. O acompanhamento da variação de produção de gases e/ou de pressão são também tópicos recentes em sensores dentro de LiBs. No entanto, devido à dificuldade e complexidade de deteção, a integração dos sensores dentro de baterias, sendo necessárias, não estão a ser exploradas.

Neste trabalho, sensores de fibra ótica híbridos baseados em Interferómetros Fabry-Perot (FPIs) e em redes de Bragg (FBGs) foram desenvolvidos e caraterizados com sucesso para discriminar simultaneamente dois fatores impactantes, pressão e temperatura, em LiBs cilíndricas para melhorar a sua operação em condições de segurança.

O sensor híbrido proposto consiste numa fibra monomodo (SMF), onde foram gravadas FBGs, fundida com um curto segmento de tubo oco cilíndrico (HCF). Para criar o FPI, a ponta da HCF foi mergulhada num polímero líquido, fotossensível (PS) a radiação ultravioleta (UV), criando três cavidades e duas interferências visíveis no espetro ótico, resultando em duas respostas Fabry-Perot. Dos quatro sensores fabricados com diferentes comprimentos de HCF, três deles foram calibrados à temperatura e à pressão. Ao seguir a variação das franjas das respostas Fabry-Perot e dos envelopes resultantes, atingiu-se maiores sensibilidades para o sensor híbrido com 175.86 μm e 26.38 μm de comprimento das cavidades através da análise dos envelopes com 31.65 nm/bar e 1.53 nm/°C, sendo a sensibilidade à pressão o maior valor registado para sensores nesta configuração.

Após a calibração, o sensor híbrido D foi selecionado e colocado dentro de uma LiB comercial LG 18650 para medir internamente os dois parâmetros. O posicionamento das FBGs e da cavidade Fabry-Perot permitem a deteção de variações de pressão no terminal positivo da bateria, e de temperatura perto dos terminais negativos e positivos, e no meio da mesma, durante os testes cíclicos galvanostáticos. Externamente, foi acrescentada uma fibra ótica com quatro FBGs para adquirir as variações de temperatura externas na cápsula protetora da bateria, sendo uma delas destinadas ao controlo da temperatura ambiente.

Os testes galvanostáticos foram realizados a diferentes temperaturas, 25.0 °C e a 40.0 °C. A deteção em tempo real das franjas Fabry-Perot e dos picos das FBGs permitiu, através de um método de discriminação matricial, obter as variações de temperatura e pressão. Resultou em leituras bem-sucedidas de temperatura e pressão, apresentando comportamentos similares a descritos pela literatura e vários comportamentos referentes aos sinais de temperatura e pressão foram identificados, tal como alguns eventos térmicos que foram detetados pelas FBGs externas.

Apesar de alguns fatores importantes ainda precisarem de algum aprofundamento para se avaliar o potencial deste sensor híbrido, como a estabilidade a longo termo, este sensor tem um enorme potencial para realizar medições simultâneas das variações de pressão e temperatura nas 18650 LiBs, durante os seus períodos de normal e anormal funcionamento.

keywords Optical fiber sensors, lithium-ion batteries, pressure, temperature, simultaneous tracking.

abstract

Society's dependency on fossil fuels is becoming a critical obstacle regarding environmental sustainability. The concentrated political power on institutions related to the fossil fuel market represents a worldwide energy dependence. Alternative energy sources could be explored to supply the energetic needs of human activity and better distribute the energy supply around the world. However, to be able to make use of these alternative energies is mandatory to consume them right away or to store them as potential energy, otherwise, they would be wasted. Multiple initiatives are investing and aiming to reduce the usage of fossil fuels by stimulating the research and development of alternative energy sources, together with energy storage development is crucial to potentialize the utilization and adoption of such alternative energies. Nowadays, rechargeable Li-ion batteries are the most adopted, scalable, and demanded energy storage devices in the world.

The scarcity of information regarding the interior of the LiBs currently hinders the improvement of the accuracy and predicting capabilities of current battery management algorithms and models, while equally limiting attempts to refine the battery thermal design due to the absence of heat-transfer information. This has led to increasing interest in spatiotemporal imaging of the thermal flows within a cell using temperature sensors. The tracking of gas production and/or pressure variations are also very recent topics of sensing inside the LIBs. However, due to the difficulty and complexity of sensing, the integration of the sensors inside the battery cells being necessary, they were not yet so explored.

In this work, hybrid optical fiber sensors based on Fabry-Perot Interferometers (FPIs) and Fiber Bragg Grating (FBG) sensors were successfully developed and characterized to discriminate two impactful parameters (pressure and temperature) internally and externally simultaneously on cylindrical lithium-ion batteries (LiB) in order to improve their operation in safety conditions.

The proposed hybrid sensors consist of a photosensitive single-mode fiber (SMF), where the FBGs were inscribed and spliced to a small section of a hollow-core fiber (HCF). To create the FPI, the HCF's tip was submerged in a UV-photosensitive polymer, creating three cavities and two observable light beam interferences in the optical spectrum, resulting in two Fabry-Perot responses. Out of four created sensors with different HCF and liquid polymer cavity's lengths, three of them were calibrated to temperature and pressure. By tracking the FP fringes and the resulting envelope shifts of the spectral responses, it achieved higher sensitivities for the hybrid sensor with 175.86 μm and 26.38 μm of cavities' lengths for the envelope analysis, with 31.65 nm/bar and 1.53 nm/°C, with the pressure sensitivity being the highest recorded value for this type of configuration.

After calibrating steps, the hybrid sensor D was selected and embedded inside a commercial LG 18650 LiB to internally dual-parameter sensing. The placement of the FBGs and the Fabry-Perot cavity allow the detection of pressure in all battery and temperature changes near the negative and positive terminals, and in the middle of the battery during several galvanostatic cycles. Externally, were also placed one optical fiber with four FBGs to acquire external temperature variations in the outer case, being one of them outside of the case to ambient temperature control.

Galvanostatic cyclic tests were performed through different temperatures, 25.0 and 40.0 °C. The online detection of the FP fringes and FBGs peaks allows, through a matrixial method discrimination, obtain the temperature and pressure variations. It resulted in successful temperature and pressure readings, resembling some occurrences presented in the available literature and other findings which concerns to pressure and temperature behaviours in different battery locations can be highlighted, like some of the thermal events were undetected by the external FBG sensors.

Although some key factors need to be further studied to understand the potential of this sensor, like the long-term stability, however this hybrid sensor design has enormous potential to perform simultaneous measurements of internal pressure and temperature shifts during normal and abnormal working conditions of an 18650 LiB.

Content

Acronyms

GHG	Greenhouse Gas
LiB	Lithium-ion Battery
BMS	Battery Management System
FOS	Fiber Optic Sensor
FPI	Fabry-Perot Interferometer
FBG	Fiber Bragg Grating
SMF	Single-Mode Fiber
HCF	Hollow-Core Fiber
MMF	Multimode Fiber
UV	Ultraviolet
VE	Vernier Effect
PS	Photosensitive
LA	Lead-Acid
AM	Active Material
NMC	Nickel Manganese Cobalt
SEI	Solid Electrolyte Interface
PTC	Positive Temperature Coefficient
CID	Current Interruption Device
MZI	Mach-Zehnder Interferometer
EFPI	Extrinsic Fabry-Perot Interferometer
IFPI	Intrinsic Fabry-Perot Interferometer
NOA	Norland Optical Adhesives
RI	Refractive Index
rSMF	reference Single-Mode Fiber
FSR	Free Spectral Range

List of Symbols

$\mathbf{M_{i=1,2}}$	Reflective surface 1 and 2
$\mathbf{R_{i=1,2}}$	Reflection coefficient of respective reflective surface
$\mathbf{T_{i=1,2}}$	Transmission coefficient of respective reflective surface
$\mathbf{L}$	Length between reflective surfaces 1 and 2
$\mathbf{E_{in}(\lambda)}$	Initial incident electric field towards the Fabry-Perot cavity
$\mathbf{E_{R1}(\lambda)}$	Electric field reflected in the first reflective surface
$\mathbf{E_{T1}(\lambda)}$	Electric field transmitted through the first reflective surface
$\mathbf{n}$	Refractive index
$\mathbf{A_{i=1,2}}$	Transmission loss of the respective surface
$\mathbf{E_{R2}(\lambda)}$	Electric field reflected in the second reflective surface
$\mathbf{E_{T2}(\lambda)}$	Electric field transmitted through the second reflective surface
$\boldsymbol{\alpha}$	Propagation losses
$\boldsymbol{\Phi}$	Phase shift caused by optical path of the light beam inside the cavity
$\mathbf{E'_{T1}(\lambda)}$	Electric field transmitted through the first reflective surface after travelling inside the cavity
$\mathbf{E^R_{FPI_1}(\lambda)}$	Total reflective electric field after one full path inside the cavity
$\mathbf{E^R_{FPI_k}(\lambda)}$	Total reflective electric field after k full path inside the cavity
$\mathbf{E^T_{FPI_k}(\lambda)}$	Total transmitted electric field after k full path inside the cavity
$\mathbf{P^R_{FPI_k}(\lambda)}$	Total reflection optical power
$\mathbf{P^T_{FPI_k}(\lambda)}$	Total transmission optical power
$\mathbf{P_{in}(\lambda)}$	Initial incident power towards the Fabry-Perot cavity

Φ_m	Phase shift of the m order peak/dip of the reflection optical spectrum
λ_m	Wavelength of the m order peak/dip of the reflection optical spectrum
$\Delta\lambda_{FP}$	Wavelength shift caused by temperature and pressure variations on the Fabry-Perot cavity
ΔT	Temperature variation
ΔP	Pressure variation
k_{FP_T}	Fabry-Perot cavity's temperature sensitivity
k_{FP_P}	Fabry-Perot cavity's pressure sensitivity
Λ	Periodicity of the phase mask used to record the Fiber Bragg Grating on the fiber optic
λ_B	Bragg's wavelength
n_{eff}	Effective refractive index of the core mode
$\Delta\lambda_{BT}$	Bragg's wavelength shift caused by temperature variations
$\Delta\lambda_{BP}$	Bragg's wavelength shift caused by pressure variations
k_T	Fiber Bragg Grating's sensitivity to temperature
k_P	Fiber Bragg Grating's sensitivity to pressure
$P_{12,11}$	Strain-optic tensor components
ν	Poisson ratio
$\Delta\lambda_{FBG}$	Wavelength shift of the Fiber Bragg Grating peak due to pressure and temperature changes
M	Determinant of the sensitivity coefficients' matrix
L_{C1}	Length of the cleaved Hollow-Core Fiber tube
L_{C2}	Length of the liquid polymer cavity
xc	Maximum/minimum value calculated of the Gauss function for the designated area of the spectrum
FP_{dips}	Fabry-Perot spectrum peaks/dips

List of Figures

List of Tables

Chapter 1- Introduction

Currently, mobility sector is experiencing a sustainability transition. Driven by global warming consequences, it is extremely important to, among other actions, lower the greenhouse gas (GHG) emissions. About 23 per cent of all GHG emissions comes from transportation [1], i.e. from internal combustion engines. Therefore, global research has intensified to increase the electromobility through the development of electrically powered vehicles, with one of the more matured and better-defined areas the usage of lithium-ion batteries (LiBs) as an alternative energy source. There are many other technologies that are also subject of studies, but, on the present stage, LiBs exhibits high power and energy density, long life cycle, high voltage and capacity, and low self-discharge rate, attracting several electronic fields to implement them [2].

However, there are some drawbacks associated with this technology, like a short range, long charging time, high cost and, to power an electric vehicle, it is required many parallel and in series batteries, as each individual cells' power and capacity is limited [2]. But, most important of all, there are some reliability and safety issues, mainly determined by the battery's chemistry composition, its operating environment, and tolerance to workload. Internal failures are related to the electrochemical instability of the cathode, the anode, the separator or, more commonly, the electrolyte, which can be controlled by voltage and temperature. Thermal runaway is a critical process, where the heat generation rate overwhelms the heat dissipation rate, causing the evaporation of chemical compounds, which consequently leads to the build-up of gases (internal pressure increases) and, possibly, a rupture and an explosion. External factors can also disrupt internal temperature, output voltage and electrochemical reactions [3] through:

- Mechanical abuse: damage to shell casing, compression, punching, cells' bending;
- Electrical abuse: overcharge or over discharge and short circuit;
- Thermal abuse: thermal shock and local heating.

It is possible to comprehend that these so-called parasitic reactions are directly related to LiB safety and reliability issues, and it is imperative to determine, during normal and abnormal working conditions, their effect to allow LiBs to perform at a normal voltage range and balancing the heat generation and dissipation rate. Therefore, it became necessary for the development of effective Battery Management Systems (BMSs) to manage, identify, and/or predict an endangering scenario and execute the proper response to take once the dangerous behaviour is observed. The measurement of external factors like voltage, strain and temperature were mainly performed with thermocouples, potentiostats, RTDs, strain gauges, among others [2], [4], [5], but with a non-optimal accuracy and incompatibilities to be integrated inside batteries because these sensors are based on electrical connections that can be influenced by electromagnetic fields. Also, due to cabling efforts and cost efficiency, it is not further developed [6]. Thus, in response to the need of a more compact technology that could reduce the overall battery cost and determine with great accuracy the aforementioned factors, a Battery 2030+ research initiative financed by European Union was created. It aims to contribute to carbon neutrality in the European Union by developing more sustainable batteries for the future, reducing the actual society's dependence on fossil fuel

energy. INSTABAT project is a member of this initiative and aims to research smart batteries and develop new methodologies to sense critical parameters within the battery cells.

Fiber optic sensors (FOS) possesses many characteristics that allow them to be a very effective alternative to the traditional electrical counterparts, due to their reduced dimensions (from µm up to mm scale), which could more easily infiltrate each battery's pack module, immunity to electromagnetic interferences, high sensitivity, capability of detecting different parameters at the same time, like strain and temperature, [7], pressure and temperature [8], refractive index and temperature [9], among others. Because of these properties, they have also shown great promise in performing internal measurements in LiBs, which becomes a very important factor to behold, because it allows a deeper understanding of the processes happening inside the battery during its charging and discharging periods [5]. In recent years, multiple types of FOS have been studied and developed, such as Fabry-Perot Interferometers (FPI) and Fiber Bragg Grating (FBG), deriving from their low production costs and easy fabrication [10]. These two simple structures represent the foundation of this work in order to simultaneously detect and discriminate pressure and temperature variations in LiBs during their operation.

1.1 State-of-the-art

In the last few years, there have been designed several FOS capable of performing temperature and pressure measurements, although the majority are not destined to discriminate them simultaneously because they only incorporate one sensing structure. In 2016, B. Xu *et al.* [11] proposed and developed a FOS based on a FPI to measure simultaneously gas pressure and temperature. The sensor consists of a single mode fiber (SMF) fusion spliced to a hollow-core fiber (HCF), with ~50 µm internal diameter, in which was inserted a glass microsphere with ~44 µm of diameter, forming three cavities and two detectable light-beam interferences. The sensor achieved different sensitivities to temperature and pressure, which means that the sensor can detect simultaneous changes of temperature and pressure, quantified in ~7.10 pm/°C and ~2.13 nm/MPa.

In 2017, W. P. Chen *et al*. [12] etched a multimode fiber (MMF) tip with an ultraviolet (UV) adhesive to create a FPI cavity to detect pressure variations, achieving an inverse behaviour as the previous work: as pressure is increasing, the spectrum response shifts the lower wavelength values, -40.94 nm/MPa. Additional tests were performed, and it was able to determine that it can also detect variations in temperature and refractive index (RI). For the latter one, it achieved -70.54 nm/RIU (refractive index units) and, although the response was not linear, it gave 0.21 nm/°C in a limited range.

A few months later, Z. Zhang *et al.* [13] reached a higher-pressure sensitivity for their FPI based sensor with a very simple, cost efficient and repeatable procedure. On the tip of a SMF, it was placed a polyvinyl chloride cap and their experiments provided a -65.50 nm/MPa of sensitivity. On the other hand, the team also performed temperature tests and it revealed -5.50 kPa/°C cross-sensitivity.

In 2020, Y. Liu and colleagues [14] proposed a similar sensor of the latter but with two different features: between the circular silicon diaphragm, it was fusion spliced a small segment of HCF to the SMF. It achieved sensitivities of 2.13 nm/kPa and 0.21 nm/°C and it could withstand

temperatures of 600.0 °C. The authors also report that, to reduce the cross-sensitivity of temperature and pressure, it can be implemented a FBG in series with the developed sensor.

In 2021, S. Zhang *et al.* [15] proposed another FPI-based FOS with a HCF fusion spliced to a SMF with a thin film at the sensors' tip, made of an epoxy glue, which was generated by a transfer method. Through a pressure pump, a microbubble with ultra-thin layer is created on the epoxy glue and, by inserting the sensor on it, it transfers to the HCF's tip. Pressure tests translated in a sensitivity of 0.26 nm/kPa and 0.38 nm/°C for the temperature one.

In February of 2022, H. Gao *et al.* [10] proposed and developed a temperature FOS based on a FPI created in a HCF filled with a UV liquid polymer. The HCF was fusion spliced to an SMF and the filling was created using a fusion splice machine, benefiting from its operating characteristics, by transferring the liquid from the tip of another SMF to the HCF. The current setup was tested, and it achieved 1.23 nm/°C. Pressure readings showed a non-linear behaviour. Then, another setup was created to introduce the Vernier effect (VE) through a parallel configuration, and it was noted that the temperature sensitivity increased more than ten times, -15.62 nm/°C.

In May of 2022, C. Lang *et al*. [16] published an article where a FOS based on the VE was developed to detect temperature variations. The sensor consisted of an FPI created in a HCF segment, which was previously fusion spliced to a SMF, by partially filling it with dimethyl silicone oil, establishing two cavities. The tip of the HCF was sealed with a thin layer of an UV-cured glue. After performing temperature tests, the results showed a maximum sensitivity of -39.21 nm/°C around 35.0 °C.

As mentioned before, the usage of FOS can be very advantageous to monitor key parameters of an operating LiB cell. J. Pinto *et al.* [17], in 2013, published the first article where FBGs were successfully integrated in LiBs to measure external temperature variations during normal and abnormal working conditions. After that, the interest in the usage of this optical sensing technology has grown a lot, due to their multiplexing abilities, higher capacity of battery integration, and to identify the thermal flows, strain, refractive index and/or pressure variations of LiBs.

In 2016, S. Novais *et al.* [18] monitored and compared internal and external temperature variations with FBG sensors, during galvanostatic cycling at 1C, 2C, 5C and 8C (charging rate), carefully placed in the center of the electrochemically active area and at the tab-electrode connection. The maximum thermal difference was achieved at 8C in the active area's center with a shift of 4.7 °C. Previous to the sensor's implementation, they were subjected to a chemical test in a conventional LiB electrolyte to assess their long-term stability. After two weeks of storage, the amount of silicon dissolved was very low and it presented no visible changes when observed under the optical microscope, thus concluding that the FBG sensitivity and response would not be compromised with long term storage in a LiB cell.

In 2017, Nascimento *et al.* [19] performed a comparative study between a single fiber optic, containing three FBGs, and K-type thermocouples to detect temperature variations in the same spots of a commercial LiB and it was obtained approximately 1.2 times higher response rate with the FBGs then with the thermocouple (4.88 °C/min to 4.10 °C/min), making the FBG a more suitable device for real-time temperature measurements.

Up to this point, researchers have focused their attention into prismatic and pouch but not to cylindrical battery cells, where it presents a greater engineering problem due to the different internal structure, assembly materials, and manufacturing methods. However, in 2018, J. Fleming *et al.* [20] proposed the in-situ measurement of temperature variations with FBG sensors, which were placed inside the battery's core and outer shell. It was able to identify a 6.0 °C and 3.0 °C difference, from both locations, at discharge and charge operating cycles.

In 2021, K. M. Alcock *et al.* [21] devised a way to attach several FBGs on a cylindrical LiB to detect in-situ temperature variations, by gluing the fiber optic on the battery's extremities. With this work, it was also shown that the temperature variations on the positive electrode tab were higher than the one detected on the negative electrode tab.

Regarding simultaneous measurement of pressure and temperature on a LiB, in 2020, Huang *et al.* [22] demonstrated that FBG sensors can be used to perform these measurements internally, where temperature variations were discriminated from a single FBG inscribed in a commercial photosensitive (PS) SMF and pressure variations were discriminated through a FBG recorded on a microstructure optical fiber, which is highly sensitive to pressure variations.

In a general way, and acknowledged by many authors, one way of avoiding the cross-sensitivity problem when performing simultaneous measurements of two parameters is to use two cascaded optical fiber infrastructures. In 2018, M. Nascimento *et al* [23] performed internal and external measurements in a Lithium-ion pouch cell to assess strain and temperature variations during a galvanostatic cycling test, with three charge/discharge cycles at 0.5 C, followed by another three at 1.0 C, and the last two at 0.25 C. The external measurements were performed by three FBGs, placed at the top, middle and bottom of the battery, and the internal measurements were performed by a cascaded FBG and FP cavity, which translated to an air cavity created between a SMF and a MMF, in the same location as the external FBGs. Some key conclusions were drawn for this work, since it was the first time that internal strain measurements were acquired. It was determined that the temperature increase is accentuated during the charge process, and at 0.3C, was detected a maximum shift of 2.7 °C and 20.0 με for the internal and external sensors placed on the top of the battery, respectively, at the end of the constant current charge step.

In 2019, Y. Liu *et al*. [24] proposed a sensor to simultaneously measure pressure and temperature by cascading a FBG sensor to a FP cavity. This cavity consists of an UV-cured glue cap on the SMF tip, created by a transfer method. The FBG was recorded near the FPI cavity in a PS-SMF without cladding to ensure that both structures sense the same temperature and pressure variations. The FBG achieved 11.6 pm/°C and was insensitive to pressure, while the FP cavity achieved 0.22 nm/°C and 2.50 nm/bar, which, by means of a sensitivity matrix, was proved that the proposed sensor can simultaneously discriminate pressure and temperature.

1.2 Motivation and goals

The energetic transition occurring nowadays has put much pressure on the automotive industry to produce and deliver better electric vehicles, in terms of autonomy, life-cycle, power, and a charging network available in almost every corner, just like the combustion engine industry has provided through the years. However, the amount of information regarding LiB behaviour

during operating conditions is very limited; it did not match the battery's pack evolution, which consequently led to several reported accidents. The traditional sensing methods by voltage and external temperature measurements are not reliable enough to ensure a good battery performance output.

Therefore, and integrated in the European Project INSTABAT, this work aims to develop a simple, fast response, effective and compact fiber optic sensor to perform internal measurements in LiBs, to assess, with greater quality and reliability, the normal and failure mechanisms that can lead to critical situations. From the several internal characteristics that can change in operating conditions, like temperature, pressure, refractive index, strain, state-of-charge, among others, for this work, it was focused only on pressure and temperature variations. So, it was proposed the development of a hybrid fiber optic sensor that can discriminate simultaneously these parameters and if it would respond effectively to the LiBs' internal environment, as it can release toxic gases that can potentially damage the sensor.

1.3 Dissertation's structure

This dissertation is divided in six chapters. In this chapter, it was presented a general overview of the progress regarding the development of FOS to characterize temperature, pressure, strain and/or refractive index variations, and some applications towards their implementation in LiBs.

Chapters 2 and 3 presents some key theoretical concepts of LiBs, namely their composition and failure mechanisms that can lead to critical situations, and how FPIs and FBGs respond to pressure and temperature changes, which is the focus of the proposed hybrid sensor. It is also demonstrated that, through a matrixial sensitivity method, it is possible to discriminate them simultaneously.

In Chapter 4, it is described the experimental steps taken regarding the hybrid sensors' manufacturing and its calibrations to pressure and temperature parameters, followed by a comparison of the fabricated sensors and the procedures necessary to embed the hybrid sensors on the 18650 LiB's core, with the following section (Chapter 5) integrating the calibration and the temperature and pressure variations during the galvanostatic cycles results, under different room temperatures.

Lastly, Chapter 6 describes the main conclusions drawn from this work and a future work is also presented to understand the full potential of this hybrid sensor to improve the LiB's safety and performance.

1.4 Main contributions

This dissertation allowed the publication of scientific works:

1) F. Freitas, L. Matuck, J. Bierlich, M. S. Ferreira, C. Marques, M. Nascimento, "Innovative hybrid optical sensing design to simultaneously discriminate pressure and temperature", *J. Phys.*: *Conf. Ser.* 2407, 012023. DOI: 10.1088/1742-6596/2407/1/012023;

2) Oral presentation in the 5th International Conference on Applications of Optics and Photonics, AOP 2022, Guimarães, with the same title name.

Chapter 2- Lithium-ion batteries

Lead-acid (LA) batteries were the first type of rechargeable batteries created and stimulated by the rapid development of the automobile industry. They became extremely relevant to the market, due to their low manufacturing cost and low self-discharge rate, namely being applied in the vehicles' starting battery. However, they are characterized with low energy density and low energy efficiency [25], therefore, in search of higher quality and more environmentally friendly solutions, lithium-ion batteries have emerged as a great candidate, by providing high energy density, low self-discharge rate, long life-cycle [26], and high capacity, voltage and power [27], characteristics that allowed them to be so attractive to be incorporated in several electronic devices, like smartphones, computers, and electrically powered vehicles [28].

There are different types of LiB configurations: flat batteries, such as pouch and prismatic cells, and rolled batteries, such as cylindrical and coin cells. Flat batteries have a higher chance of causing a short circuit and deformation due to the successive layers of negative and positive electrodes. On the other hand, cylindrical batteries are mechanically more stable and have a higher energy/volume ratio. However, there have been many reports of LiBs related incidents over the years, which were mainly due to short circuits, mechanical abuse, battery overcharging, and design and manufacturing defects. For example, a well-known case relates to the mass product recall, in 2016, of Samsung's smartphone Note 7, due to the dozens of acknowledged explosions and/or fires. In electric vehicles, there have been also some reported cases of battery malfunction leading to fires [25].

Since this work is inserted in the European project INSTABAT and it focuses of LiBs that are used in electric vehicles, this work will only focus on cylindrical batteries, more specifically, the 18650 model [29].

2.1 Lithium-ion batteries: manufacturing, composition, and operating principles

In the 1980s decade, Yoshino developed the first productionally viable LiB by combining a lithium cobalt oxide, $LiCoO_2$, cathode with a graphite, C_6, anode [26], [27]. It completely revolutionized technological progress by means of a higher energy and power density, safety, and life cycle. Its costs have also dropped by about 5 times from the early 2000s to pre-pandemic days. However, through the years, manufacturing processes have not received much attention from researchers to simplify and reduce their costs. In general, the production of LiB cells involves five major steps (Figure 1) [28]:

- **Mixing and coating**: both sides of metal foils are coated with a previously mixed electrode (active material, AM) slurry and compressed for the slitting process, to cut it into the specific dimensions of the battery;
- **Winding the positive and negative electrodes, and separator**: to avoid short circuit, a separator is placed between the positive and negative electrodes. Then, the layered structure is rolled to form a cylindrical shape;

- **Inserting the wound center pin into the battery case and filling it with the electrolyte**: since the separator and electrolyte are microporous, and any moisture can result in the electrolyte's decomposition, a series of procedures are followed to ensure that their pores are filled with the electrolyte. A center pin is inserted to, among other functionalities, fix and support the electrode assembly;
- **Sealing the battery case**;
- **Formation and aging**: identify any manufacturing defects and age the cell.

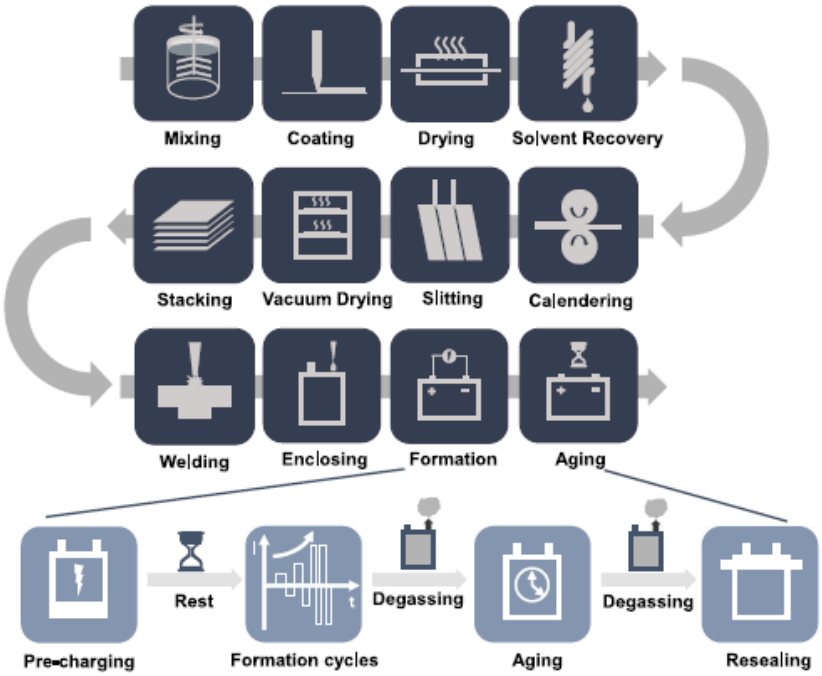

Figure 1 - Stages for lithium-ion batteries' manufacturing. [26]

A schematic of the internal composition of a cylindrical LiB is presented in Figure 2, more precisely, of the 18650 model, commercially used in the EV battery pack.

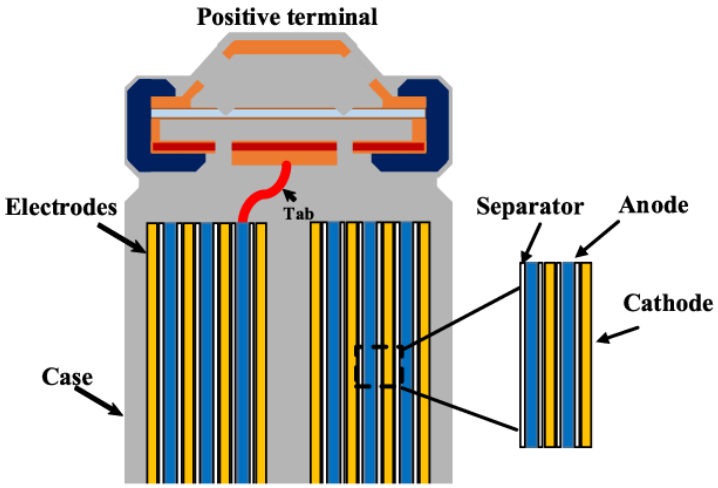

Figure 2 - Internal composition of an 18650 lithium-ion battery cell. [30]

As seen previously, a basic LiB cell consists of a cathode – positive electrode - (metal oxide) and an anode – negative electrode - (graphite), isolated with a separator (polyolefin membrane), rolled to create a cylindrical shape, in direct contact with an electrolyte containing lithium salt in an organic solvent, and inserted in a tubular aluminum case [27], [30], [31]. The separator is microporous to allow the exchange of lithium ions, but not electrons. When the battery is being charged, Figure 3 (a), the electrons are released from the cathode and move externally towards the anode; simultaneously, the lithium ions travel from the cathode, but through the separator and the electrolyte, to the anode. When the battery is discharging, Figure 3 (b), the opposite occurs: the electrons travel externally and the lithium-ions from the anode, through the electrolyte, to the cathode [31], [32].

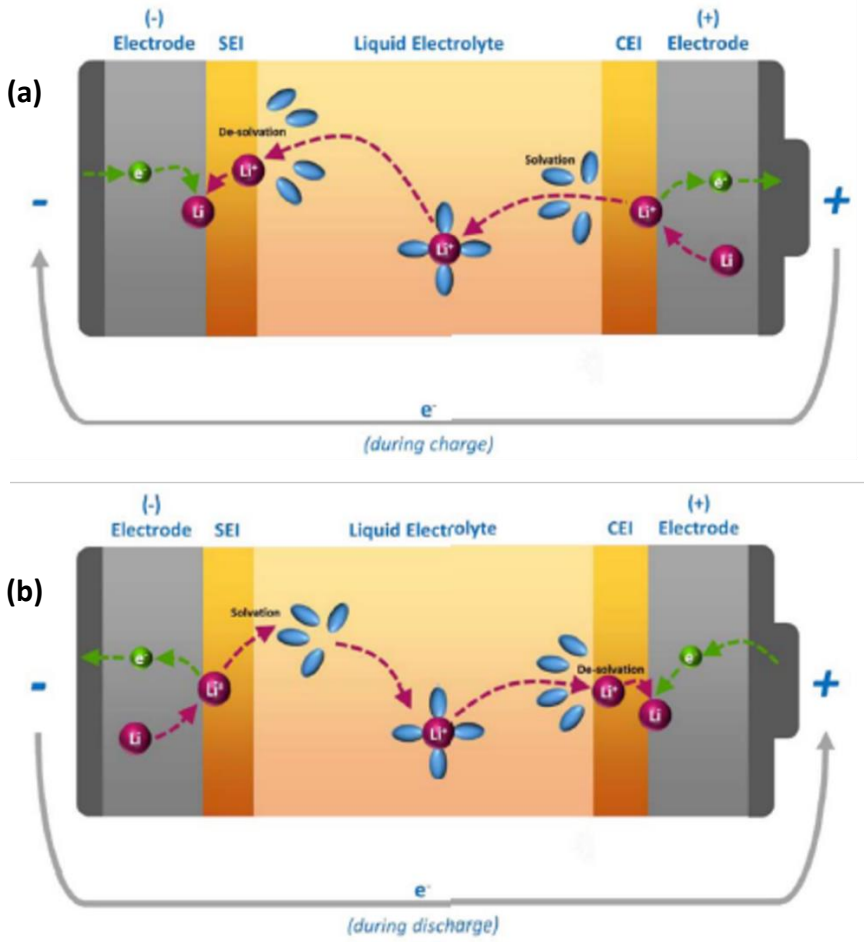

Figure 3 - General operating principle of a cylindrical lithium-ion battery during its (a) charging step, where a solvated Li^+ is turned into Li in the electrode by accepting an electron from the negative (-) electrode; and (b) discharging step, where the de-solvation process occurs at the cathode. Adapted from [32]

Graphite is a good choice as an anode material because it must characteristically have low potential, high reducing power and high mechanical strength to withstand any form of abuse. Regarding the cathode, there are a bunch of materials being currently tested and inserted in LiBs: lithium cobalt oxide, lithium nickel manganese cobalt (NMC), $LiNi_xMn_yCo_zO_2$, and lithium iron phosphate, $LiFePO_4$, for example, but each of them contains their own set of drawbacks that can ultimately lead to failures.

There are a few criteria that need to be filled for a material to be selected as an electrolyte. It should:

- allow the passage of the lithium ions but not electrons;
- not undergo degradation over working potentials;
- not react with other battery components;
- be thermically stable over a set of temperatures;
- be non-toxic, sustainable, and environmentally and economically friendly.

As for separators, it must be a ~40 % porous electrochemically stable material, and have high absorption and retention capabilities, with a good thermal and dimensional stability, like polyethylene terephthalate, polyacrylonitrile, or polybutylene terephthalate [33].

2.2 Lithium-ion batteries: failure mechanisms

Although LiBs are widely used in various applications, if they are subjected to stress situations, it can result in a chain reaction that leads to potentially dangerous situations. Figure 4 shows the complex network of cause and effect that can compromise their operation, in a safety regime. The failure of a LiB can be induced by intrinsic and/or extrinsic factors.

Thermal runaway is a very critical stage for the LiB. It directly affects the battery voltage, temperature, and pressure, and it is extended when the heat dissipation rate is lower than the heat generation rate. In this way, the development of FOS with higher accuracy and faster response time, to perform internal measurements, is greatly necessary because of some particularities of the thermal runaway [25]:

- the output voltage remains unchanged, and it only drops sharply a few seconds after the uncontrollable temperature increase began;
- the thermal runaway can begin in a specific spot of the battery and propagate to the entire battery; additionally, if integrated in a LiB battery pack, if one cell is affected by thermal runaway, the same effect can be triggered on the rest of the cells due to overheating.

Therefore, the traditional methods of measurements are not very effective in detecting the thermal runaway; for example, a multimeter to detect voltage variations between the cathode and the anode, or by using only one thermocouple to monitor the central region of batteries to estimate their overall temperature.

Another way of detecting when thermal runaway is happening is by analysing pressure and/or refractive index variations due to the gas production. During normal working conditions in a LiB with liquid electrolyte, it can produce gases like CO_2, CO, CH_4 and O_2. With the uncontrollable temperature phenomenon, it can release CO_2, CO, CH_4, C_2H_6, C_2H_4 -all compounds dependent of the used electrolyte- and H_2, which is directly related to the thermal runaway effect. Also, the cathode can release O_2, a flammable compound, increasing the risk of fire.

The separator, a porous material that is applied to purposely not cause internal short circuit, can trigger them: if the temperature inside the battery cell matches the separator's melting

point, its pores can close, which will block the passage of lithium-ions through it. If the separator collapses, both electrodes can connect with each other and lead to an internal short circuit. Mechanical abuse can damage the separator and cause the growth of lithium dendrites. If it leads to the contact of the electrodes, it consequently causes a short circuit and thermal runaway. [33].

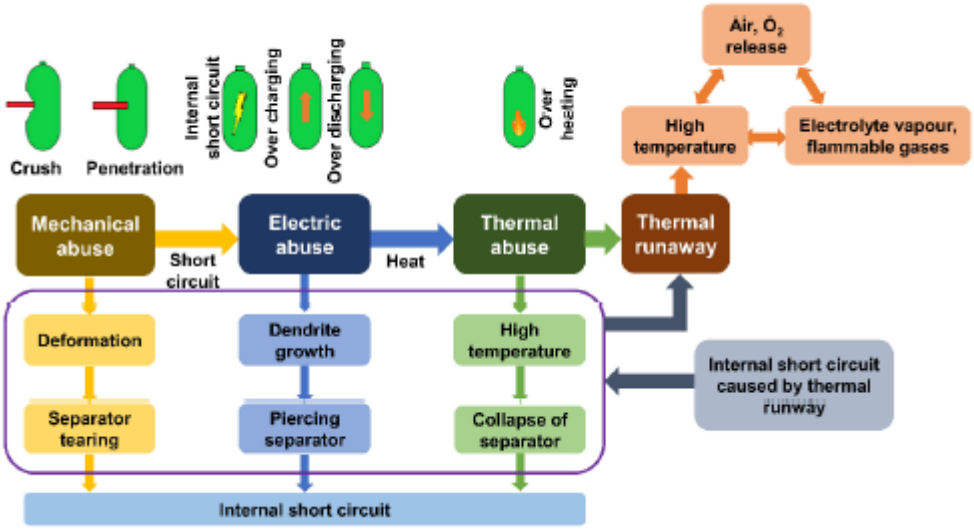

Figure 4 - Failure mechanisms in lithium-ion batteries. [33]

Due to the carbon-based anode and the electrolyte reactions, it can occur two situations: Solid Electrolyte Interface (SEI) layer formation and dendrite growth. Several side reactions can occur during charging and discharging processes. The electrolyte has certain solvents that can react with the carbon-based anode, thus creating a SEI that results in an irreversible capacity and power loss by reducing the electrode reaction. This layer itself does not lead to thermal runaway, but if the internal temperature reaches its fusion point, the decomposition of this layer can release flammable hydrocarbon gases, causing thermal runaway. If a LiB is rapidly charged at sub-operating temperature range, it can lead to dendrite formation, which puncture the separator and lead to an internal short circuit [25]. Despite this, the battery case holds some safety components to minimize the effects of thermal runaway, Figure 5, like vents, positive temperature coefficient (PTC) thermistors, and current interruption device (CID).

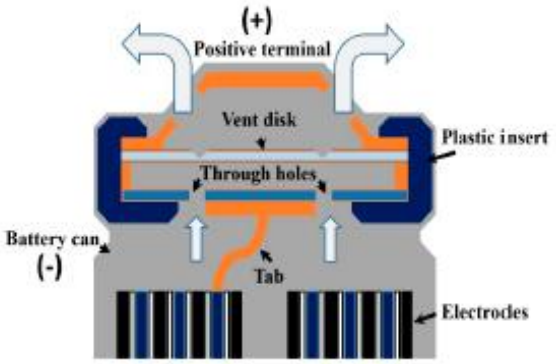

Figure 5 - Typical 18650 lithium-ion battery's cap. [28]

The vents act as pathways for the controlled release of gases, while the PTC protects the battery against short circuit as its resistance increases with temperature, thus decreasing battery's current. If the pressure inside the battery surpasses a certain threshold, the positive tab is broken, disconnecting the positive terminal with the rest of the cell assembly. If the PTC thermistor is activated, the battery can recover; on the other hand, if the battery's conditions trigger the vent and/or the CID, it is not reusable anymore [30].

Chapter 3- Optical fiber sensors- Theoretical approach

As seen previously, the most common and reliable temperature sensing device is the FBG which, due to their small dimensions, fast response, and immunity to electromagnetic interferences [34], presents as a great sensor to perform external and internal measurements in LiBs. Interferometer-based fiber optic sensors have been implemented in fiber sensors because components that allow the measurement of the optical phase shift induced by the changing environmental parameter presents high sensitivity, which can be performed through Mach-Zender interferometers (MZIs) and FPIs. Since the implementation of MZI is less practical than a FPI, given by the fact that a MZI requires two directional couplers that acts as a light beam splitter/recombining element, and after S. Petuchowski *et al.* [35] published the first work where a FPI was implemented on a SMF, the FPI attracted a lot of attention from researchers because of their simple manufacturing processes, immunity to environmental noise, high versatility, and, as shown, [36], by coupling it with a FBG, it can discriminate simultaneously several parameters. This setup is very advantageous for the simultaneous discrimination of temperature and pressure since the FBG is sensitive to temperature and practically insensitive to pressure at low ranges [37], while the FPI can be influenced by both through its cavity length shift.

There are two types of FPIs: extrinsic (EFPIs) and intrinsic (IFPIs) and their main difference stands from the location of the cavity. In EFPIs, the microcavity is created outside of the fiber optic core, allowing the light beam to interfere directly with the ambient characteristics; on the other hand, the IFPIs' cavity is manufactured internally, in the fiber optic's core, inhibiting the direct contact of the light beam with the ambient [18], and, regarding this work, since during charging and discharging cycles toxic gases can be released from the battery's components, an IFPI is a more viable solution to protect the HCF's core from them.

3.1 Fabry-Perot interferometers sensors

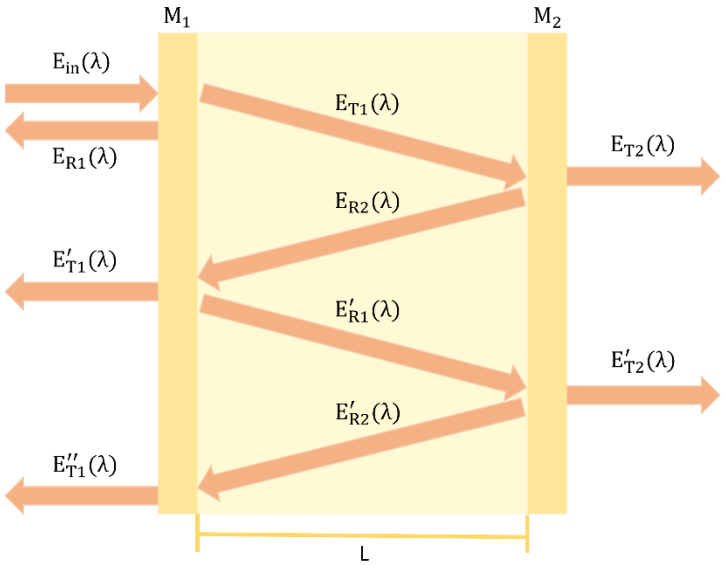

Figure 6 - Schematic of the operating principle of the Fabry-Perot interferometer.

A FPI is an optical instrument based on the multiple interference of confined beams [38] in a small cavity formed by two reflective surfaces, $M_{i=1,2}$, with reflection and transmission intensity coefficients of $R_{i=1,2}$ and $T_{i=1,2}$, respectively, distanced L, Figure 6.

Assuming that both surfaces are parallel and the light beam travels through a SMF core, when an electric field, $E_{in}(\lambda)$, is focused perpendicularly towards the first surface, it will reflect, $E_{R1}(\lambda)$, and transmit, $E_{T1}(\lambda)$, to the cavity, with refractive index (RI) n, which can be represented by equations 1 and 2, respectively:

$$E_{R1}(\lambda) = \frac{\sqrt{R_1}E_{in}(\lambda)}{\sqrt{2}}, \tag{1}$$

$$E_{T1}(\lambda) = \frac{\sqrt{1-A_1}\sqrt{1-R_1}E_{in}(\lambda)}{\sqrt{2}}, \tag{2}$$

with $A_{i=1,2}$ the transmission loss of the respective surface. The latter electric field will propagate inside the cavity and perform a reflection, $E_{R2}(\lambda)$ (equation 3), and transmission, $E_{T2}(\lambda)$ (equation 4), in surface $i = 2$:

$$E_{R2}(\lambda) = \frac{\sqrt{1-A_1}\sqrt{1-R_1}E_{in}(\lambda)}{\sqrt{2}}\exp(-\alpha L)\sqrt{R_2}\exp\left[-j\left(\frac{\phi}{2}-\pi\right)\right], \tag{3}$$

$$E_{T2}(\lambda) = \frac{\sqrt{1-A_1}\sqrt{1-R_1}\sqrt{1-A_2}\sqrt{1-R_2}E_{in}(\lambda)}{\sqrt{2}}\exp(-\alpha L), \tag{4}$$

being $\exp(-\alpha L)$ the propagation losses inside the cavity, and $\left(\frac{\phi}{2}-\pi\right)$ the phase shift, with $\frac{\phi}{2} = \frac{2\pi n L}{\lambda}$ and $(-\pi)$ the phase shift caused by the reflection between the less refringent medium (air cavity) and the higher refringent medium (SMF core). The electric field $E_{R2}(\lambda)$ will propagate inside the air cavity and, once again, will be partially reflected and transmitted, $E'_{T1}(\lambda)$, given by equation 5:

$$E'_{T1}(\lambda) = \frac{(1-A_1)(1-R_1)E_{in}(\lambda)}{\sqrt{2}}\exp(-2\alpha L)\sqrt{R_2}\exp[-j(\phi-\pi)]. \tag{5}$$

After one cavity's course, the total reflected electric field, $E^{R}_{FPI_1}(\lambda)$, can be quantified by equation 6:

$$E^{R}_{FPI_1}(\lambda) = \frac{\sqrt{R_1}E_{in}(\lambda)}{\sqrt{2}} + \frac{(1-A_1)(1-R_1)E_{in}(\lambda)}{\sqrt{2}}\exp(-2\alpha L)\sqrt{R_2}\exp[-j(\phi-\pi)]. \tag{6}$$

So, from the several light beam interactions, it is possible to identify that a reflection on each surface $i = 1,2$ causes an attenuation of $\sqrt{R_1}\exp\left(-j\frac{\phi}{2}\right)$ and $\sqrt{R_2}\exp\left(-j\frac{\phi}{2}\right)$, respectively; each optical path through the cavity promotes an attenuation of $\exp(-\alpha L)$; and the electric field that passes through the reflective surfaces suffers an $\sqrt{1-R_{i=1,2}}\sqrt{1-A_{i=1,2}}$ attenuation. Also, if the electric field is reflected between a lower density medium to a higher one, it suffers a $(-\pi)$ shift in phase. So, if the electric field inside the cavity performs k two-reflection-cycles, the final reflective electric field output, $E^{R}_{FPI_k}(\lambda)$, can be given by equation 7:

$$E^{R}_{FPI_k}(\lambda) = \frac{E_{in}(\lambda)}{\sqrt{2}}\left[(1-A_1)(1-R_1)\exp(-2\alpha L)\sqrt{R_2}\exp[-j(\phi-\pi)]\sum_{k=0}^{\infty} s^k + \sqrt{R_1}\right], \quad (7)$$

while the final transmitted electric field output, $E^{T}_{FPI_k}(\lambda)$, is given by equation 8:

$$E^{T}_{FPI_k}(\lambda) = \frac{E_{in}(\lambda)}{\sqrt{2}}\left[\sqrt{(1-A_1)}\sqrt{(1-R_1)}\sqrt{(1-A_2)}\sqrt{(1-R_2)}\exp(-\alpha L)\sum_{k=0}^{\infty} s^k\right]. \quad (8)$$

with $s = \sqrt{R_1 R_2}\exp(-j\phi - 2\alpha L)$. Since $|s| < 1$, the sum operator can be approximated to (equation 9):

$$\sum_{k=0}^{\infty} s^k = \frac{1-s^k}{1-s} \underset{s^k \ll 1}{\Longrightarrow} \sum_{k=0}^{\infty} s^k \approx \frac{1}{1-s}. \quad (9)$$

Thus, equations 7 and 8 can be simplified to equations 10 and 11, respectively:

$$E^{R}_{FPI_k}(\lambda) = \frac{E_{in}(\lambda)}{\sqrt{2}}\left[\frac{B\exp[-j(\phi-\pi)]}{1-C\exp(-j\phi)} + A\right], \quad (10)$$

$$E^{T}_{FPI_k}(\lambda) = \frac{E_{in}(\lambda)}{\sqrt{2}}\left[\frac{D}{1-C\exp(-j\phi)}\right], \quad (11)$$

with

$$\begin{cases} A = \sqrt{R_1} \\ B = (1-A_1)(1-R_1)\exp(-2\alpha L)\sqrt{R_2} \\ C = \sqrt{R_1 R_2}\exp(-2\alpha L) \\ D = \sqrt{(1-A_1)}\sqrt{(1-R_1)}\sqrt{(1-A_2)}\sqrt{(1-R_2)}\exp(-\alpha L) \end{cases}. \quad (12)$$

The total reflection and transmission optical power, $P^{R}_{FPI_k}$ and $P^{T}_{FPI_k}$ (equations 13 and 14, respectively), can be obtained through equations 7 and 8:

$$P^{R}_{FPI_k}(\lambda) = \left|E^{R}_{FPI_k}(\lambda)\right|^2 = \left[\frac{A^2 + (-AC-B)[2A\cos(\phi) + (-AC-B)]}{1-C[2\cos(\phi)-C]}\right]P_{in}(\lambda), \quad (13)$$

$$P^{T}_{FPI_k}(\lambda) = \left|E^{T}_{FPI_k}(\lambda)\right|^2 = \left[\frac{D^2}{1-C[2\cos(\phi)-C]}\right]P_{in}(\lambda), \quad (14)$$

with $P_{in}(\lambda) = \frac{E_{in}(\lambda)^2}{2}$, the initial electric field power emitted onto the FP cavity.

As seen from the graph in Figure 7, the $P^{R}_{FPI_k}$ maximum occurs at $\pm\pi, \pm 3\pi, \ldots, (\pm\pi \pm 2\pi m)$, and the minimums at $0, \pm 2\pi, \ldots, (\pm 2\pi m)$, and vice-versa for $P^{T}_{FPI_k}$. By analysing equation 14:

$$\frac{P^{T}_{FPI_k}(\lambda)}{P_{in}(\lambda)} = \begin{cases} \frac{D^2}{C^2+1}, \text{if}\cos(\phi) = 0 \rightarrow \text{minimum} \\ \frac{D^2}{C^2-2C+1}, \text{if}\cos(\phi) = 1 \rightarrow \text{maximum} \end{cases}, \quad (15)$$

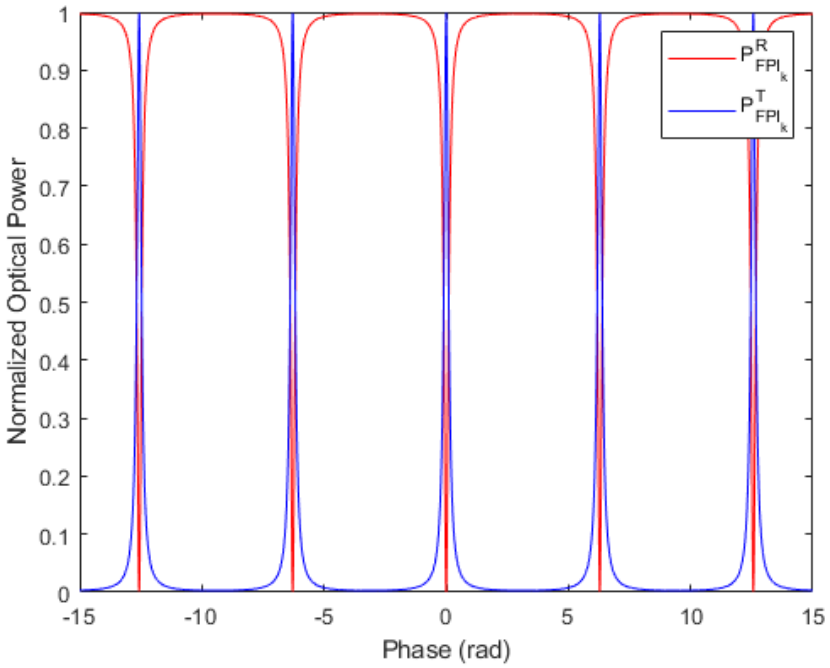

Figure 7 - Normalized reflection and transmission optical power loss in terms of phase shift: n = 1.455, $R_{1,2}$ = 0.9, L = 200 μm, $a_{1,2}$ = 10^{-5}, α = 10^{-7}, simulated in Matlab®.

so, $\frac{P^R_{FPI_k}(\lambda)}{P_{in}(\lambda)}$ presents minimums for $\cos(\phi) = 1$, which gives (equation 16)

$$\frac{4\pi nL}{\lambda} = 2\pi m \Leftrightarrow \lambda = \frac{2nL}{m}. \tag{16}$$

Since the distance between two minimums and maximums is, in terms of phase, 2π:

$$\phi_m - \phi_{m+1} = 2\pi \Leftrightarrow \frac{4\pi nL}{\lambda_m} - \frac{4\pi nL}{\lambda_{m+1}} = 2\pi \Leftrightarrow \lambda_{m+1} - \lambda_m = \frac{\lambda_m \lambda_{m+1}}{2nL}, \tag{17}$$

then, it is possible to determine the length of the cavity by analysing the wavelength of two adjacent dips of the reflection spectrum from equation 18:

$$L = \frac{\lambda_m \lambda_{m+1}}{2n(\lambda_{m+1} - \lambda_m)}. \tag{18}$$

Therefore, the interferometric frequency can be adjusted by changing the optical path length of the light beam, by means of RI changes and/or the distance between both reflective surfaces, since these parameters are related to ϕ, the propagation losses inside the cavity $\exp(-\alpha L)$, and the distance between two adjacent dips/peaks of the spectrum, which ultimately will instigate variations in the reflection spectrum. So, since some external factors, like pressure and temperature variations, can reflect in n and L changes, a FP cavity can perform as a pressure and temperature sensor [39]. If the wavelength shifts, $\Delta\lambda_{FP}$, are proportional to the mentioned external factors, ΔT and ΔP, then $\Delta\lambda_{FP}$ can be quantified through equation 19:

$$\Delta\lambda_{FP} = k_{FP_T}\Delta T + k_{FP_P}\Delta P, \tag{19}$$

where k_{FP_T} and k_{FP_P} represents the sensitivity coefficients of the FP cavity with temperature and pressure variations, respectively.

3.2 Fiber Bragg Grating sensors

A FBG translates to the periodic changes in the RI of the PS-SMF core when a monochromatic light beam is focused through a phase mask with a periodicity, Λ. This causes the reflection of a specific wavelength, so-called Bragg wavelength, λ_B, and the transmission of all other wavelengths of the lasers' spectral window. This wavelength is given by (equation 20)

$$\lambda_B = 2n_{eff}\Lambda, \tag{20}$$

which is related to the phase mask period, Λ and the effective refractive index of the core mode, n_{eff}. External factors can influence the λ_B output. For temperature changes, ΔT, it reflects on variations in the n_{eff} and changes in the gratings' periodicity, which causes a wavelength shift, $\Delta\lambda_{BT}$, quantified through equation 21 to 24:

$$\Delta\lambda_{BT} = \left|\frac{\partial\lambda_B}{\partial T}\right|\Delta T \tag{21}$$

$$\Leftrightarrow \Delta\lambda_{BT} = 2\left[n_{eff}\frac{\partial\Lambda}{\partial T} + \Lambda\frac{\partial n_{eff}}{\partial T}\right]\Delta T \tag{22}$$

$$\Leftrightarrow \Delta\lambda_{BT} = \lambda_B\left[\frac{1}{\Lambda}\frac{\partial\Lambda}{\partial T} + \frac{1}{n_{eff}}\frac{\partial n_{eff}}{\partial T}\right]\Delta T \tag{23}$$

$$\Leftrightarrow \Delta\lambda_{BT} = k_T\Delta T, \tag{24}$$

where k_T represents the temperature sensitivity. For pressure changes, ΔP, the wavelength shift, $\Delta\lambda_{BP}$ is characterized through equation 25 to 27:

$$\Delta\lambda_{BP} = \left|\frac{\partial\lambda_B}{\partial P}\right|\Delta P \tag{25}$$

$$\Leftrightarrow \Delta\lambda_{BP} = \lambda_B\left[-\frac{(1-2\nu)}{E} + \frac{n_{eff}^2}{2E}(1-2\nu)(2P_{12}+P_{11})\right]\Delta P \tag{26}$$

$$\Leftrightarrow \Delta\lambda_{BP} = k_P\Delta P, \tag{27}$$

where k_P represents the pressure sensitivity, $P_{12,11}$ the components of the strain-optic tensor, E the Young's modulus of the fiber, and ν the Poisson's ratio. When a FBG is experiencing both external variations, the wavelength shift, $\Delta\lambda_{FBG}$, corresponds to the sum of both factors (equation 28) [34], [40], [41]:

$$\Delta\lambda_{FBG} = \Delta\lambda_{BT} + \Delta\lambda_{BP} \Leftrightarrow \Delta\lambda_{FBG} = k_T\Delta T + k_P\Delta P. \tag{28}$$

3.3 Simultaneous discrimination by a sensitivity matrixial method

If both sensors present a good linearity rate, it is possible to combine equations 19 and 28 into a sensitivity matrix (equation 29), which is used to determine the individual wavelength shifts of the resulting reflection spectrum when it is affected by, in this case, temperature and pressure variations [23], [42], [43]:

$$\begin{bmatrix}\Delta\lambda_{FBG}\\ \Delta\lambda_{FP}\end{bmatrix} = \begin{bmatrix}k_{FBG_P} & k_{FBG_T}\\ k_{FP_P} & k_{FP_T}\end{bmatrix}\begin{bmatrix}\Delta P\\ \Delta T\end{bmatrix}. \tag{29}$$

If k_{FBG,FP_P} and k_{FBG,FP_T} are known, then, by performing the matrix's inversion, equation 30, it is possible to obtain the temperature and pressure relative variations, by inserting the wavelength shift corresponding to each sensor, i.e., the FBG peak shifts and the spectrum peak/dip shifts:

$$\begin{bmatrix}\Delta P\\ \Delta T\end{bmatrix} = \frac{1}{M}\begin{bmatrix} k_{FP_T} & -k_{FBG_T}\\ -k_{FP_P} & k_{FBG_P}\end{bmatrix}\begin{bmatrix}\Delta\lambda_{FBG}\\ \Delta\lambda_{FP}\end{bmatrix}, \tag{30}$$

with $M = k_{FBG_P}k_{FP_T} - k_{FP_P}k_{FBG_T}$ the matrix determinant, which must be a non-zero number to allow simultaneous measurement [23].

Chapter 4- Optical fiber hybrid sensor's design

In this work, it was proposed the conception of a FOS to enable the simultaneous discrimination of two impactful factors on a LiB to its safety and reliability: temperature and pressure, which, as seen previously, can be achieved by coupling two sensing structures, a FBG to a FPI. As FPI is sensible to both factors, and FBG is practically insensitive to pressure in low ranges [37], it can act as a temperature discriminator and help on decoupling wavelength shifts due to pressure or temperature variations. Therefore, their characteristics allow the creation of a suitable hybrid sensor with great potential to detect individual changes of temperature and pressure. In Figure 8, it is represented a scheme of the hybrid sensor designed, with 1 FBG recorded in a PS-SMF coupled to a FPI with two distinguishable cavities: one with air, and the other with a cured UV-glue. By comparing the sensor´s configuration and the ones presented in Section 1.1, it is possible to acknowledge some similarities between them, like the main frame of the hybrid sensor, however it possesses some key differences that allow it to be an innovative one. The ultimate goal of this work is to detect pressure and temperature variations inside a LiB during charging and discharging operating conditions. Therefore, after manufacturing the proposed sensor, LiBs were carefully drilled, in University of Aveiro, i3N laboratory, to place the optical fiber hybrid sensors inside their core.

Figure 8 - Schematic of the proposed hybrid sensor, containing one FBG, embedded in a PS-SMF, and an IFPI manufactured inside a HCF with an UV-photosensitive polymer.

4.1 Hybrid sensor's fabrication

The first stage relates to the manufacturing of the main structure. The hybrid sensor fabrication started by splicing (by using the splice machine Fujikura, FSM-40S) a commercial PS-SMF to an HCF, produced in Leibniz Institute of Photonic Technology, with an internal diameter of ~96 µm. The PS-SMF needs to have a minimal length of 6.5 cm to match the height of an 18650 LiB, useful to later record three FBGs. In both fibers, the cladding was previously removed to reach an external diameter of ~125 µm.

Due to the different internal diameters of the mentioned fibers, it is not possible for the fusion splice machine to execute a splice with an automatic alignment. Instead, it is implemented a manual alignment, as schematized in Figure 9, and it proceeds as follow: the PS-SMF is clamped to the machine's left motor, with a single dimension manual displacement (x-axis) and a reference SMF (rSMF) is clamped on the opposite arm, which is connected to a motor with three-dimension manual displacement (x-, y-, and z-axis). Both fibers need to have a perfect cut (fiber sections perpendicularly to the propagation axis (90°)) and be cleaned in order to be suitable for fusion splicing. An initial automatic alignment is performed by the machine (a); rSMF is removed after shifting the right motor to the furthest position from the PS-SMF, and the HCF segment is placed and moved until it reaches a position ~250.0 µm off-site from the fusion spot (0.0 µm on the

scheme) (b); the left motor moves the PS-SMF close to the latter position and, through the two-direction displacement (y- and z-axis) of the right motor, it is performed a manual alignment, by visualizing the process through the equipment's inboard camera (c); with both segments aligned, an electric arc (15 bit of power during 500 ms) is applied to the PS-SMF, fusing both interfaces (d).

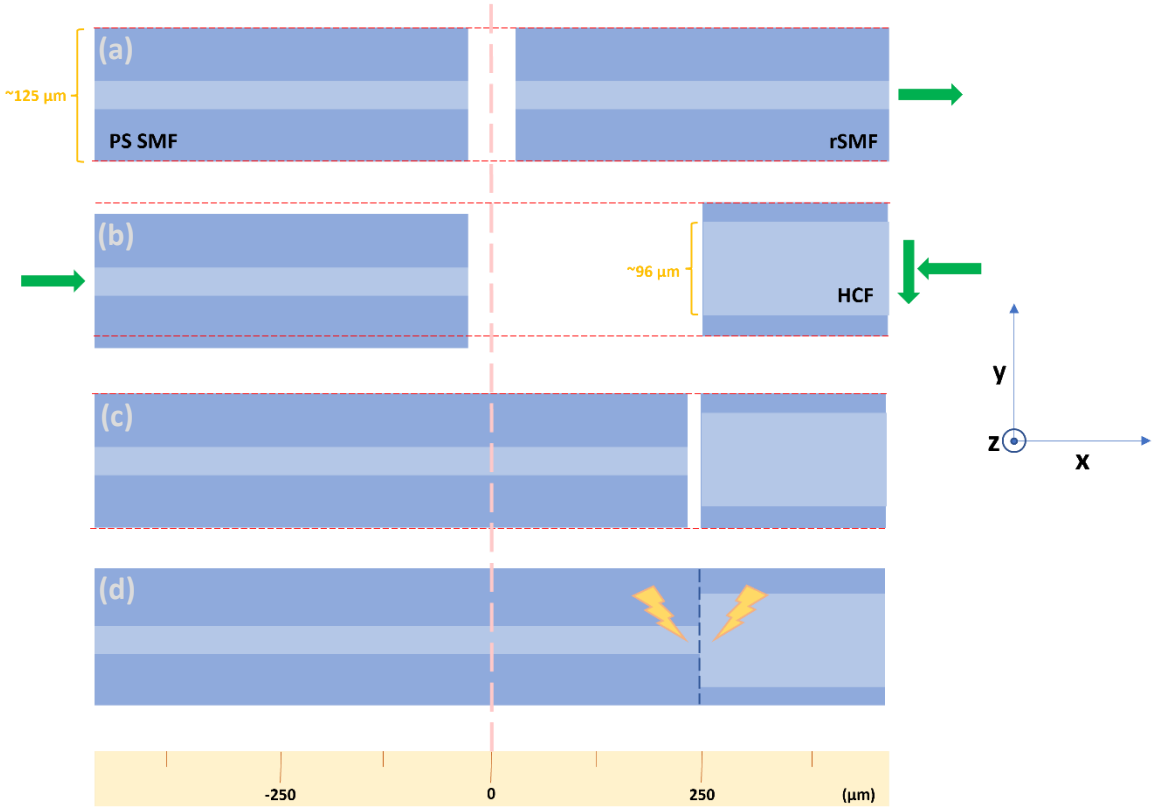

Figure 9 - Schematic of the manual alignment for the fusion splicing of the PS-SMF and the HCF.

The next step is to shorten the length of the HCF to L_{C1} in a fiber cleaver. This procedure was performed in order to achieve different lengths of the HCF tip to compare their spectral responses. Due to the difference in the core's refractive index of the PS-SMF and the HCF, it was possible to detect where both fibers were spliced.

The third stage involves the creation of the FP cavities. For that, it was assembled the setup presented in Figure 10 (left). The fiber optic frame (PS-SMF and HCF, Figure 10 (right)) were held by a clamp -in a cladding segment to ensure that it would not break by its resting position- connected to a vertical micrometer to allow their vertical translation. It was assembled into a structure fixed on the table to inhibit any kind of displacement. Beneath the sensor's tip and supported by a lifting table, was placed a glass slide containing a liquid polymer's single droplet, Figure 11 (a). To assess if liquid polymer was entering the HCF, the pigtail was connected to an optical interrogator (Hyperion si155, LUNA®, Atlanta, GA, USA), with a spectral range of 1460.0 to 1620.0 nm, wavelength accuracy of 8.0 pm and operating at 100.0 Hz, to observe the online spectral responses. By using the vertical micrometer, the HCF tip was dipped in the droplet and, through the superficial tension of the HCF's internal surface, the UV-glue was inserted inside the HCF's tip, Figure 11 (b). Since the entire HCF's tip section is dipped at the same time, there will be no air circulation, which means its cavity cannot be entirely filled with the liquid polymer, thus creating three distinguishable

cavities, Figure 11 (c). Since FP cavities lengths interfere with the interferometric frequency of the reflection spectrum, the liquid polymer's cavity needs to be cured under the direct incidence of an UV-lamp (from 10 to 15 minutes with 5.0 W/cm^2).

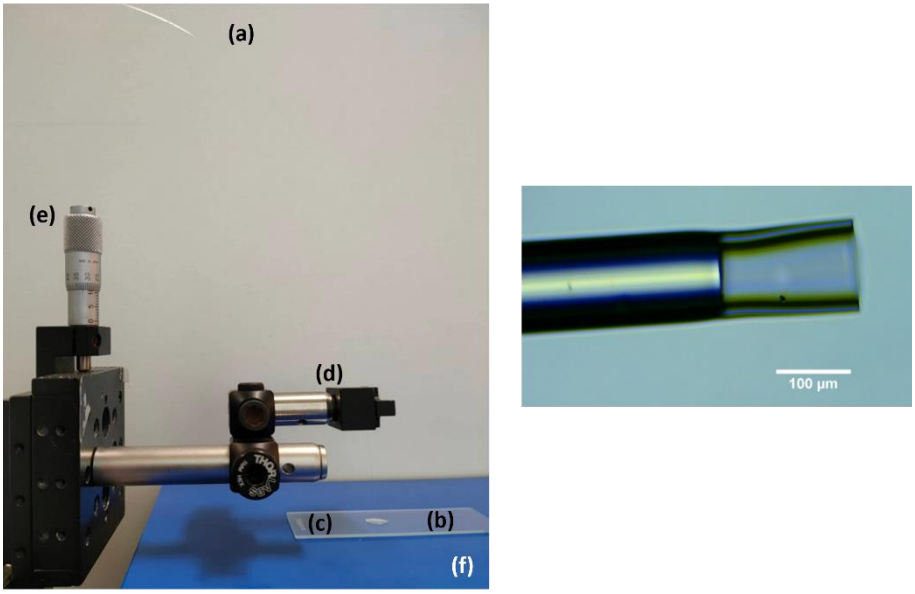

Figure 10 - (left) Experimental setup of the liquid polymer's cavity manufacturing processes: (a) fiber optic frame; (b) glass slide; (c) droplet of NOA (Norland Optical Adhesive) 85; (d) clamp; (e) vertical micrometer; (f) lifting table. (right) Fiber optic frame under the optical microscope, with a x10 magnification.

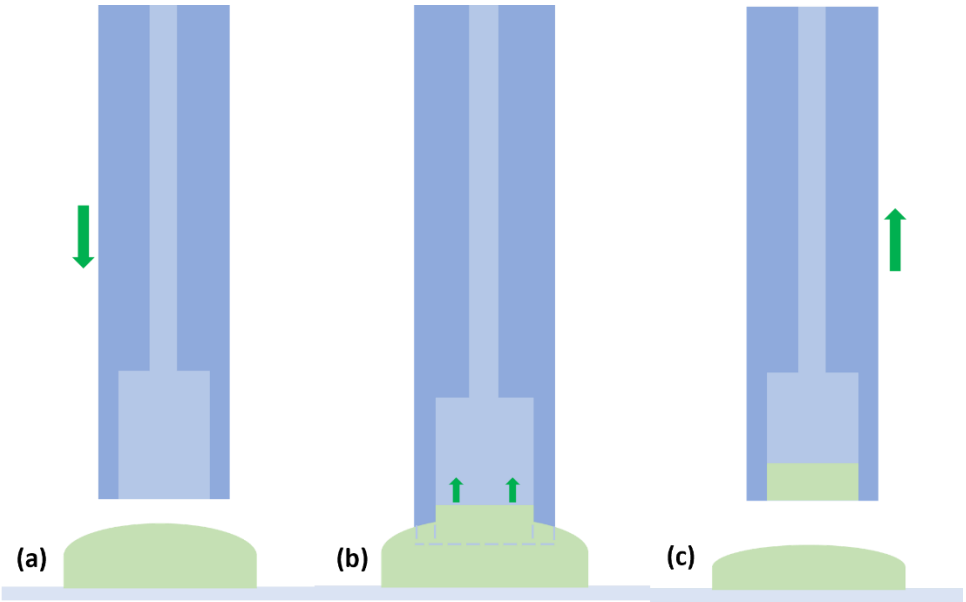

Figure 11 - Schematic representing the Fabry-Perot cavity formation with the UV-photosensitive polymer: (a) vertical translation of the fiber optical frame; (b) dipping in the droplet and consequent filling of the HCF; (c) removal of the HCF's tip and creation of the Fabry-Perot cavity.

The final stage comprehends the recording of the FBGs in the PS-SMF, which were inscribed by a pulsed Q-switched Nd:YAG laser system (LOTIS TII LS-2137U Laser, Minsk, Belarus) lasing at the fourth harmonic (@266 nm) and focusing the beam in the fiber with a plano-convex cylindrical lens (working length of 320 nm) (Figure 12). In order to obtain FBGs with different wavelength peaks,

four phase masks with different grating periods (1056, 1060, 1067, and 1077 nm, approximately) were used. The wavelength peaks obtained were around 1526, 1532, 1540, and 1554 nm, being the FBG with the lowest wavelength peak localized near the fiber's tip.

Figure 12 - UV-laser facility of Nanophotonics and Optoelectronics i3N laboratory.

4.1.1 Specifications for the Fabry-Perot interferometer's production and hybrid sensor's characterization

To reach a verdict on several characteristics of the hybrid sensor, some experiments were performed regarding the splice fusion between the PS-SMF and the HCF, the cleaved HCF's length, and the liquid polymer used to create one of the FP cavities.

The first one is related to the fusion splice parameters between PS-SMF and HCF. By applying the electric arc directly to the fibers' junction, it resulted in a deformation of the fibers interface core. So, two key modifications were performed: the electric's arc power and time windows were adjusted, ending up with 15 bit of applied power during 500 ms, and the fibers junction spot should be shifted from the electric arc's location, to decrease the impact of the fusion splice, but not so far to not fusion splice both fibers' sections.

Some tests were also performed in order to select the UV-glue to produce the hybrid sensor. In this way, several liquid polymers were tested: NOA 85, NOA 86, NOA 139, NOA 146H, NOA 148, with their main characteristics (refractive index, viscosity at room temperature, temperature range, and curing time) summarized in Table 1. NOA 85 achieved a higher efficiency in terms of completed sensor due to its curing time, viscosity, and RI. This adhesive presented a shorter curing time which allowed the creation of a FP cavity, and good spectral response was obtained due to the higher optical losses, which will facilitate the FBG visibility in the final spectrum. The spectral response was followed during the curing time (Figure 13). It was observed that the free-spectral range (FSR) has increased with the curing time, driven by the regression of the liquid polymer's cavity over time, supported through equation 17. So, if the UV-photosensitive polymer did not cure before reaching the ultimate possible length to withstand, it would open, thus ceasing to exist.

Table 1 - Characteristics of the tested UV-photosensitive polymers.

Norland Optical Adhesive	85	86	139	146H	148
Refractive Index (RIU)	1.46	1.55	1.39	1.46	1.48
Viscosity at 25 °C (cps)	200	200 to 300	865	40	1500 to 2000
Temperature range (°C)	-15 to 90	-125 to 125	-15 to 90	-15 to 90	-15 to 90
Curing time	~10 minutes	1 week	Needs an inert atmosphere	Needs two curing procedures	Needs an inert atmosphere

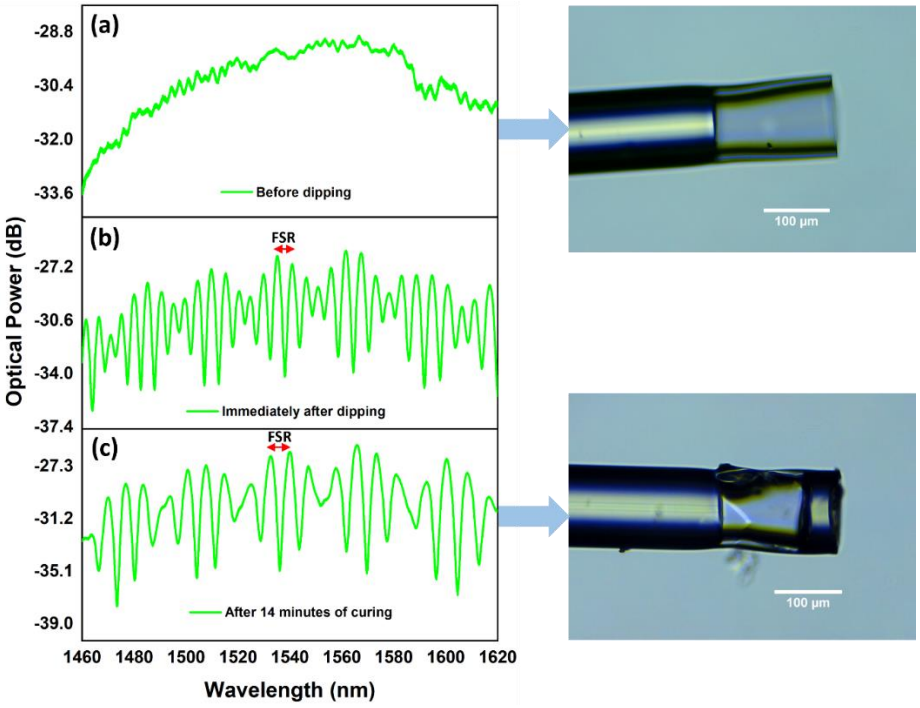

Figure 13 - FSR evolution of Sensor B during the curing process: (a) before dipping and respective fiber optic frame photograph, with x10 magnification; (b) immediately after dipping; (c) at the end of the curing process (14 minutes) and respective photograph, with x10 magnification.

To identify the optimal HCF's length range, different sensors were manufactured to evaluate how its length influences the interference reflection spectrum. In Figure 14 (a), (b), (c) and (d), it is presented four sensors, A, B, C and D, respectively, and their respective spectral responses, with their cavities' length summarized in Table 2 (measurements performed with ImageJ® software from a x10 magnification photograph with the optical microscope). As seen from the four spectrums, the envelope analysis is well defined for the presented L_{C1} lengths' range. Therefore, the goal for the HCF's length range was established to be between 150 and 300 µm for the available spectral emission window. Using equation 18, we can determine the theoretical cavities' lengths by using two adjacent dips of the spectrum, for L_{C1}, and two adjacent minimums/maximums of the

upper envelope. In Table 2 is represented the selected data to the formula. With the theoretical values, and comparing with the measured values, it shows a good approximation.

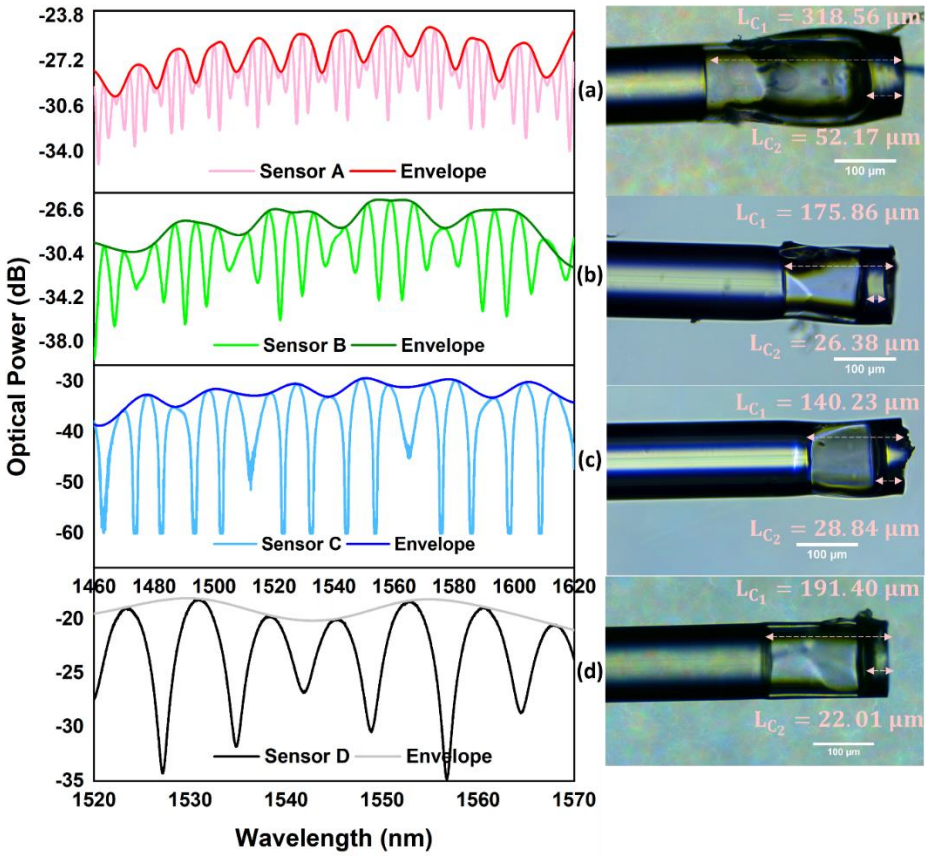

Figure 14 - Optical spectrum of (a) sensor A, (b) sensor B, (c) sensor C, and (d) sensor D, with the respective photograph, with x10 magnification, with the respective C1 and C2 cavities' lengths.

Table 2 - Summary of the cavities' length of sensor A, B, C, and D.

FP cavity	RI	Sensor	Wavelength (nm)		Theoretical value (µm)	Measured value (µm)
C1	1.00	A	1538.42028	1542.23942	310.62	318.56
		B	1518.07086	1533.02649	157.05	175.86
		C	1512.46387	1521.48985	127.48	140.23
		D	1530.94817	1538.30932	159.97	191.40
C2	1.46	A	1585.68185	1593.72772	53.74	52.17
		B	1530.09154	1564.91011	23.63	26.38
		C	1517.25972	1544.76364	29.84	28.84
		D	1529.73885	1554.87681	32.40	22.01

Analysing the proportion between the theoretical lengths of the liquid polymer's cavity, L_{C2}, and the cleaved HCF tube, L_{C1}, the highest proportion was achieved for the sensor C (0.2341), followed by sensor D (0.2025), sensor A (0.1730), and for sensor B was achieved the lowest value (0.1505). Furthermore, by analyzing the corresponding spectrums (sensor A, B and C acquired with Hyperion si155's optical interrogator, and sensor D spectral response was recorded with sm125-500, Micron Optics Inc., Atlanta, GA, optical interrogator, with a sample rate of 2.0 Hz and a wavelength accuracy of 1.0 pm, with a spectral window between 1520 and 1570 nm) and the cavities' lengths, it is possible to assume some correlations: sensor A's spectrum presents 11 visible envelope minimums (calculated with Origin® software), while sensor B, and C presents between 5 to 6 countable ones; regarding the spectral response itself, sensor A attains more than 40 peaks, sensor B has 19, and sensor C has 15 peaks. Therefore, and considering the proportion between L_{C1} and L_{C2} measured values of each sensor, it can be deducted that the reflection spectrum's envelope is related to L_{C2} and reflection spectrum's peaks/dips is related to L_{C1}. This can be proved through equation 17, by replacing λ_m with the envelope/adjacent dips minimums/maximums and the Fast Fourier Transform (FFT) of the graphs, Figure 15 (a), (b), (c), and (d). Since sensor A has longer cavities, both detected frequencies are higher. Then, for example, regarding the interferometric frequency corresponding to L_{C1}, sensor C should have higher frequency than sensor B and D; however, it is not visible from the graphics, but it can be attributed to the low resolution (8.0 pm) of the first interrogator.

From these graphics, it is visible two peaks, meaning that the optical spectrum of the sensors is due to two light beam interference. Due to the concaved shape of the liquid polymer's cavity, the light beam interference, caused by the cavity created between PS-SMF and HCF interface, and air-HCF and UV-glue-HCF interface, is not visible, thus not influencing the reflection spectrum.

This work, unfortunately, did not comprehend a study about the amount of time or HCF section submerged in the droplet and how it influences its final length. However, it is deductible that the amount of liquid polymer inserted in the HCF can be directly related to L_{C1}'s length: the greater its length, the higher quantity of liquid polymer that can infiltrate the HCF.

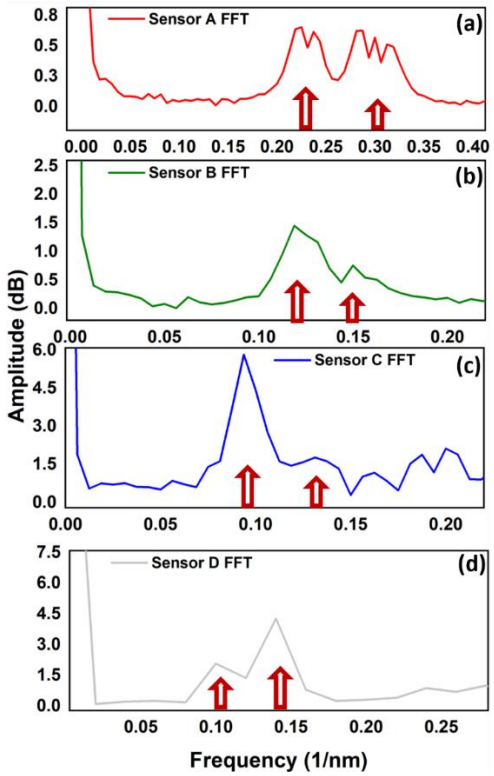

Figure 15 - Fast Fourier Transform of (a) sensor A, (b) sensor B, (c) sensor C, and (d) sensor D, simulated in Origin®.

After that, the FBGs were then recorded on the PS-SMF section. This procedure turned out to also be very delicate due to the technical characteristics of the recording technique because it was not possible to clamp the fibers tip, containing the FP cavities, potentially damaging it. So, sensor A used as a proof-of-concept, in which was recorded just one FBG (1554 nm, with 27.6 mJ of input laser power for 2 minutes) with 8.0 mm length, 1.0 cm apart from the HCF's tip. As the fiber's tip is heavier, it would cause a slight bend to it, which can lead to a non-perfect FBG inscription, with each periodic RI changes having a non-90° angle with the fiber core's normal vector. However, the final result was satisfactory, and the FBG peak was presented in the optical spectrum (Figure 16).

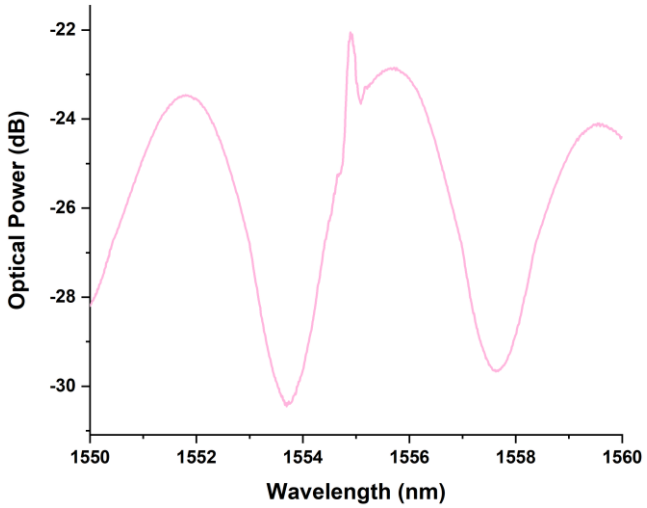

Figure 16 - FBG inscribing test, with the 1077 nm phase mask, for the hybrid sensor A.

As the main goal of this work is to perform and simultaneously discriminate internal measurements of pressure and temperature inside a cylindrical LiB, and to get a better understanding of its normal and failure mechanisms, it was designed the inscription of 3 FBGs, with a length of 0.8 cm, and evenly spaced 1.0 cm apart. So, on Hybrid Sensor B, C and D were already implemented 3 FBGs. Therefore, Hybrid Sensors B, C and D are suitable of detecting temperature and pressure variations near the positive terminal, through a 1526 nm FBG (hybrid sensor B and C) and 1532 nm FBG (hybrid sensor D) and FP cavities; in the middle of the battery, through the 1540 nm FBG (hybrid sensor D) and the 1532 nm FBG (hybrid sensor B and C); and near the negative terminal, by a 1554 nm FBG for all hybrid sensors. By recording a FBG close to the FP cavities, 1.0 cm apart, it is more plausible that both sensors are subjected to the same surrounding environment.

4.2 Setup for the hybrid sensors' calibration

With the manufactured sensors and before their integration in the LiB, it was needed to characterize them, to understand how they behave with temperature and pressure changes and obtain their respective sensitivities. Temperature calibrations were performed in a climatic chamber (Model LC64, from WeissTechnik®, Supplylab, Lisbon-Portugal, with an operating range between -70 and 180°C), Figure 17 (a), and in steps of 2.0 °C, from 22.0 °C to 30.0 °C, it was recorded two types of data: the spectral responses after stabilizing the chamber's internal temperature - approximately 25 minutes apart- and the FBGs wavelength peaks at 1 second acquisition rate. To control the temperature of the chamber, another FBG sensor was also used.

Pressure calibrations were performed by using a stainless-steel pressure chamber, controlled with a digital manometer, as shown in Figure 17 (b), for a range of 0.0 to 4.0 bar, in steps of 0.2 bar. In both cases, the spectral responses were acquired with the previously mentioned optical interrogator (Hyperion si155, LUNA®, Atlanta, GA, USA) and processed with Kolibri® software.

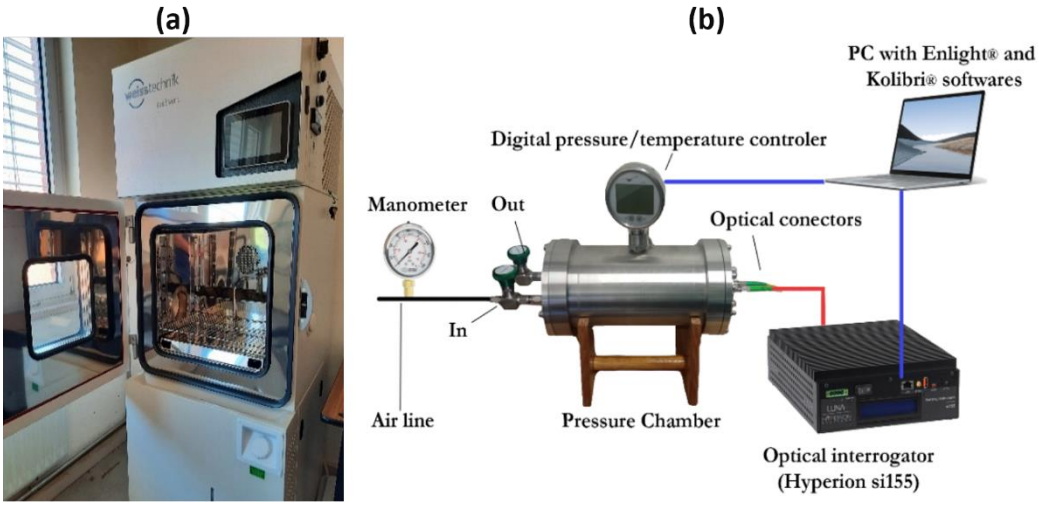

Figure 17 - Climatic chamber used for the temperature calibration and (b) experimental setup used for the pressure calibration.

4.3 Lithium-ion battery sensors' instrumentation

After characterizing the sensors to pressure and temperature parameters, the next step corresponds to the most dangerous and delicate task of this work: inserting the optical fibers with the hybrid sensors inside the commercial 18650 rechargeable INR18650 MH1 3200 mAh LiBs (18.0x65.0 mm, approximately), manufactured by LG Chem company, with a nominal and cutoff voltage of 3.63 V and 2.5 V, respectively. For this battery, the anode is composed by graphite, the cathode by lithium nickel manganese cobalt (NMC), and the involucre material is composed by aluminum.

To avoid disassembly of the batteries and associated potential performance impact, a unique drilling process was developed for the 18650 format cells. Similar to previous works [44], [45], the negative terminal is preferred as the entry point for instrumentation. This avoids disrupting the safety features often included in cylindrical cells (pressure vent) and poses less risk of short circuits (the aluminum protection is, in fact, connected to the negative terminal). Eventual risks in this process are also associated with gases releasing when the drill is very large because, if the drill is not correctly positioned, it can damage some internal components; plus, the presence of oxygen (O_2) can react with the electrolyte and cause an ignition and, in an extreme situation, a battery's explosion.

In this work, a custom process based around friction drilling as reported in literature was used, where the material is formed and pushed (not cut) [48]. Furthermore, no swarf (dust or waste material) enters the cell during the process, which reduces the risk of short circuit or contamination within the cell. There is no reliance on magnetism, which could drop larger debris into the cell. In this way, for the drilling process a mini milling machine (MF70 Proxxon, Germany) was used and selected by offering programmable feed rates and adjustable rotation speeds in a package sufficiently compact to use inside of a glove box. So, to ensure that the experiment will not be compromised, all the equipment necessary was placed, for 24 hours, in a nitrogen enriched glove box (<10 ppm O_2), at the Department of Chemistry of University of Aveiro.

To perform the drill hole, a mark is carefully placed by hand on the negative terminal surface of the LiB to serve as guidance to drill precisely where the mark is, which indicates the LiB's core position. The battery is placed on the pre-fabricated supporting structure, with the negative terminal facing up, and gently compressed laterally to hold it when drilling. This compression has also to be done carefully because, as shown in Figure 18 (left), is another mechanism that leads to LiB failure. The drill is positioned into the vertical drill axis; when so, it is turned on and slowly descended until it contacts with the negative tab surface and completely penetrates it. The drill is removed and turned off just as it leaves the LiB. Nitrogen gas is blown into the surface by a pipette Pasteur to remove any excess aluminum particles that have been left with the drilling. For the friction drilling process, it was used a 0.9 mm diameter drill and operated at a low rotation speed of 5000 rpm at 1 mm/s feed rate, and it removes sufficient material to form a thread in the cell's end. These drill setup parameters were experimentally determined to offer the optimum hole formation, with minimal damage. This process avoids the need to permanently affix sensors into the cell (i.e., via gluing, which was found to be unreliable, because some substances could leak into

the cell) and it also enables repeatable instrumentation across different batches of cells. Importantly, sensors can be fully prepared prior to entry into the glove box, allowing precise alignment of FOS.

The next step involves the sensor placement inside the performed battery hole. The supporting platform is shifted laterally to give more space for the sensor placement. As the tip of the sensor is made out of glue and there may be some glue in the HCF's external surface, the placement procedure is arduous because it does not pass through the aperture very easily, which could damage the sensor's head. The sensor was eventually inserted inside the LiB until it reached the 6.5 cm mark.

After this, the battery's hole was sealed with a high temperature resistance epoxy resin mixture (Axton®). Until it solidified, the instrumented batteries remained in the glove box from 24h, to not allow any gas to leak the batteries. Figure 18 (right) demonstrates a LiB perforated and sealed, with the sensor placed internally.

During all the drilling process and hybrid sensors integration an online visualization of the hybrid sensors spectral responses was followed. However, spectral changes were not observed, which means that the hybrid sensors head was not in contact with the LiB's core case.

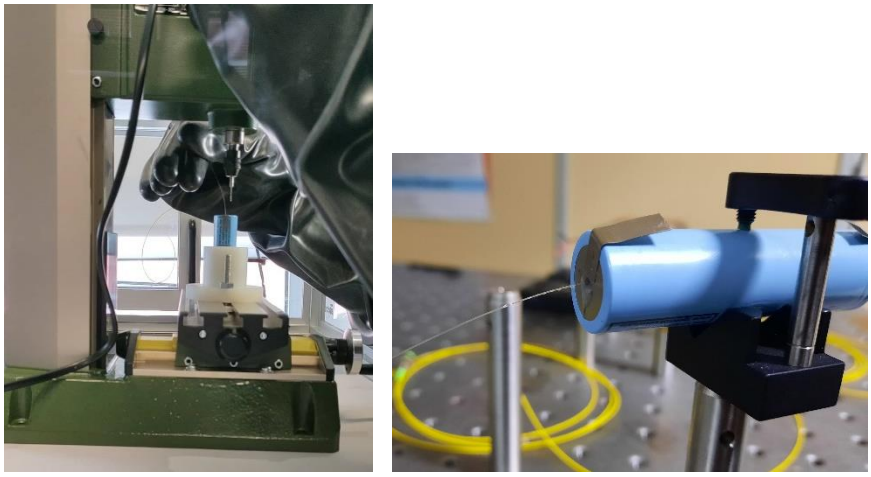

Figure 18 - (left) Experimental setup of the drilling process. (right) Lithium-ion battery instrumented with the internal optical fiber hybrid sensor.

Thus, with the hybrid sensor in place, it is now possible to acquire the pressure and temperature variations, through wavelength shifts, inside the LiB. Additionally, and applying a similar setup used in [23], four FBGs were inscribed in a single PS-SMF and were placed on the LiBs outer case to obtain the temperature variations, being the 1532, 1541 and 1554 nm FBG applied for the anode, middle of the battery and cathode readings, respectively, and the 1561 nm FBG, away from the battery, used to control the ambient temperature, Figure 19. Thermal paste was added to three external FBGs to increase the conductivity between the battery's outer case and the referenced FBGs.

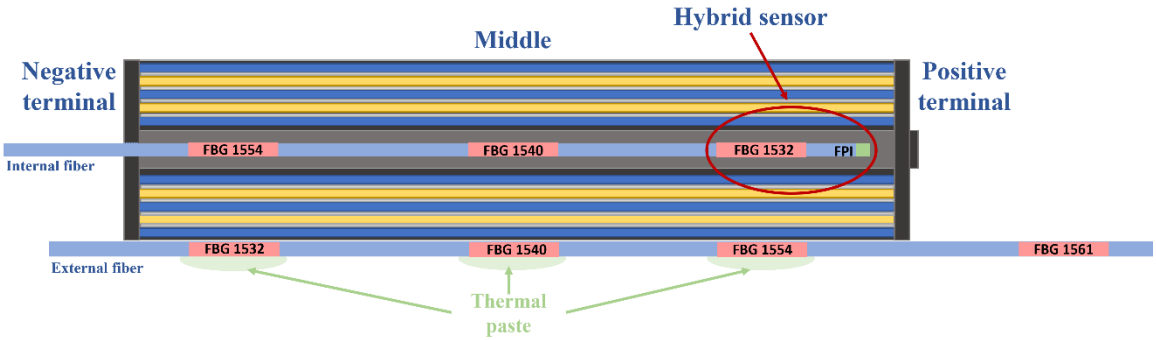

Figure 19 - Schematic of hybrid sensor D inside the 18650 lithium-ion battery, with four external FBGs: FBGs 1532, 1540 and 1554 containing thermal paste, and FBG 1561 used to control the ambient temperature. Not at scale.

4.4 Galvanostatic cyclic tests

To simulate operating conditions on a LiB, it was performed two galvanostatic cyclic tests with a potentiostat (SP-150e Potentiostat, ±1 A, from BioLogic®) with different ambient temperatures on the climatic chamber (previously mentioned), 25.0 °C to simulate normal conditions, and 40.0 °C for abnormal conditions. At each test, were performed four charges and discharges cycles at maximum current, ±1 A, at ~0.3 C-rate -the 18650 LiB has 3200 mAh of capacity-. At the beginning of the test, it was set a rest time of two hours to ensure that the ambient temperature was stable, and, at the end of each charge/discharge step, was set a 15-minute rest to stabilize the battery [23], totalizing, each test, to approximately 31 hours. From these tests, were recorded the corresponding spectral responses every 20 seconds and each FBG internal and external peaks 2 seconds apart from the optical interrogator Hyperion si155, LUNA®, Atlanta, GA, USA. Battery's regarding data, like voltage, capacity, current, were recorded using the EC Lab® software, with steps of 2 seconds.

Chapter 5- Results and discussion

To characterize the developed hybrid sensors to temperature and pressure, their spectral responses were analysed through the Origin® software. For FBGs calibration, was applied the "Peak - Gauss" function to obtain the wavelength ("xc" in Figure 20) to the corresponding spectrum's maximum value in the selected range (yellow area). For the FP_{dips} calibration, before analysing them with the same method as the FBGs, in each spectral response was applied a filter to remove the envelope effect from the spectrum, because by analysing the original spectrum evolution, it was noticed that the spectral fringes are affected by the envelope signal. For the envelope analyses, it was used the "envelope" function available in Origin® before applying the "Peak – Gauss" function. With all the "xc" values saved, it was possible to determine the sensors' sensitivities to temperature and pressure.

The data analysis of the calibration processes, and the hybrid sensors data´s during the galvanostatic cyclic tests were performed by, in first place, applying a band pass filter to all respective spectral responses, except for the FBG data, which was not done in any of the referenced works. Without the band pass filter, the sensitivities achieved were much different and, in some cases, the response was symmetrical. Some further tests need to be made to assess what is the most correct way, because, for this work, it was noted that the lower interferometric frequency (envelope) causes the spectral peaks to shift more than their linear behaviour when close to the envelope minimums. However, since the data was in accordance with the available information about pressure and temperature variations in 18650 batteries, it is assumed that this was the correct procedure. As hybrid sensor A was used as a proof-of-concept for the FBG inscribing, in this stage, it was calibrated the hybrid sensors B, C and D.

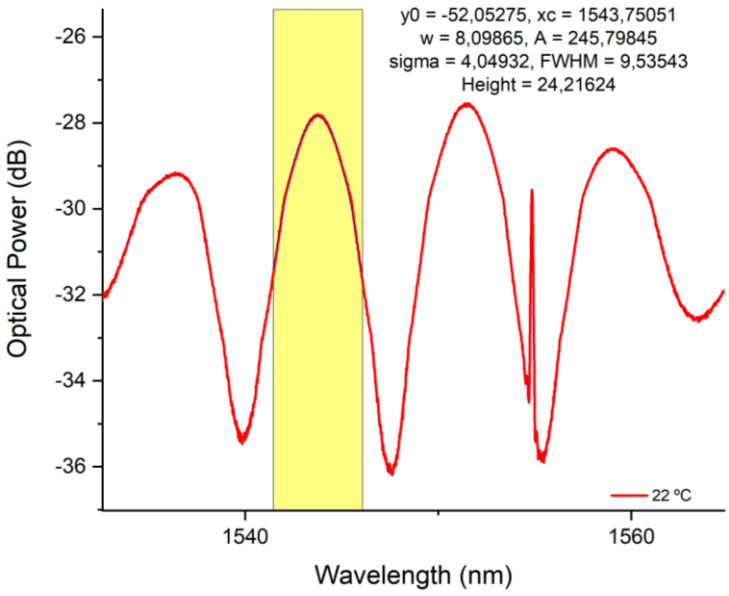

Figure 20 - Application of Gauss's function to determine the wavelength corresponding to the dip's maximum, through Origin® software.

5.1 Hybrid sensors' temperature characterization

In figures 21 (a), 22 (a), and 23 (a) are represented the full reflection spectrum at a temperature calibration's step, between 22.0 and 30.0 °C for hybrid sensor B and C, in steps of 2.0 °C, and 25.0 to 50.0 °C in steps of 5.0 °C for the hybrid sensor D, because this sensor was meant to be introduced in the LiB and a greater temperature range for calibration is advised. The arrow in each graph represents the spectrum points used to obtain the FP temperature sensitivity, k_{FP}, and how the spectrum progressed at each iteration. In figures 21 (b), 22 (b), and 23 (b) are represented the corresponding sensitivities, with the summarized results explicit in Table 3.

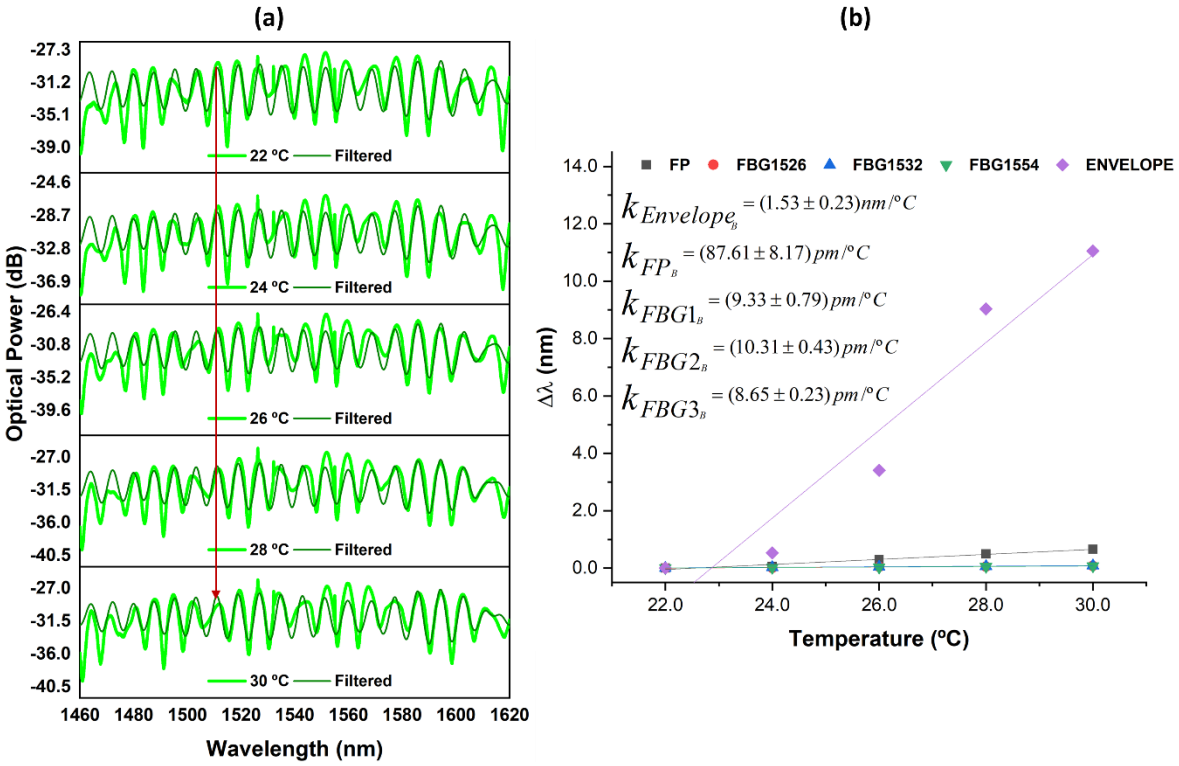

Figure 21 - (a) Spectral response at each step and (b) linear fits of the hybrid sensor B for the temperature calibration.

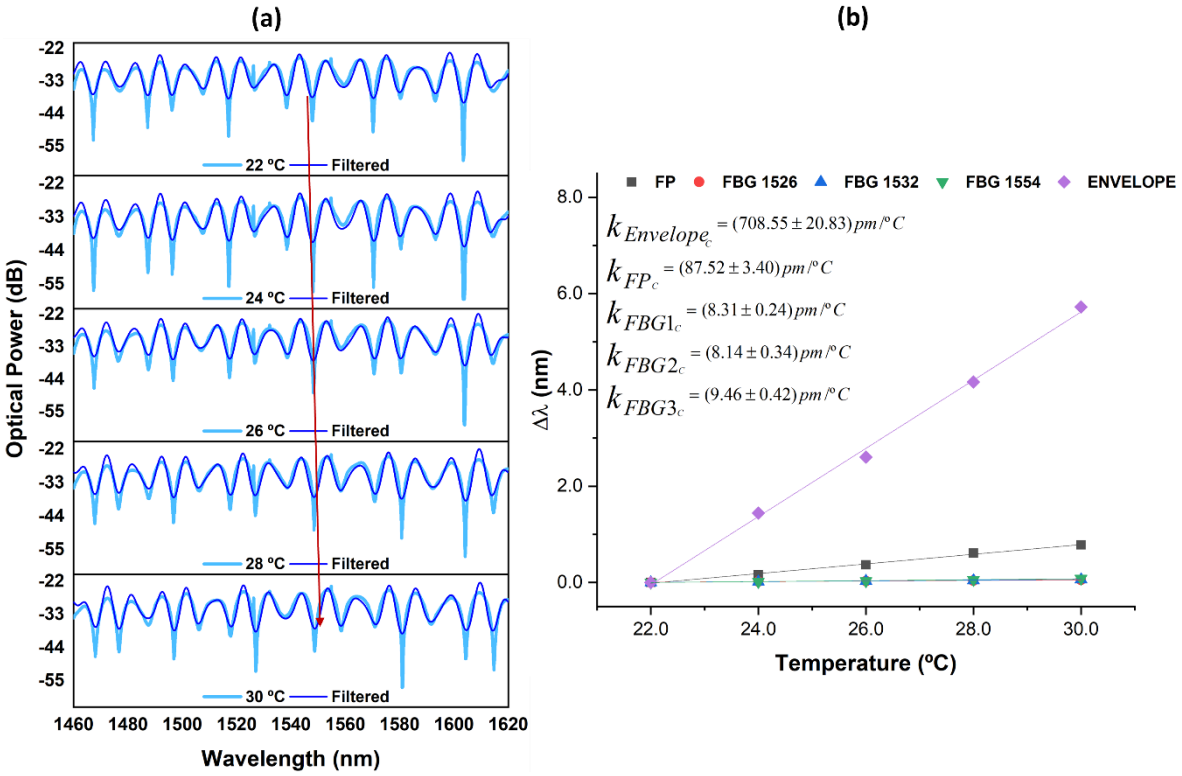

Figure 22 - Spectral response at each step and (b) linear fits of the hybrid sensor C for the temperature calibration.

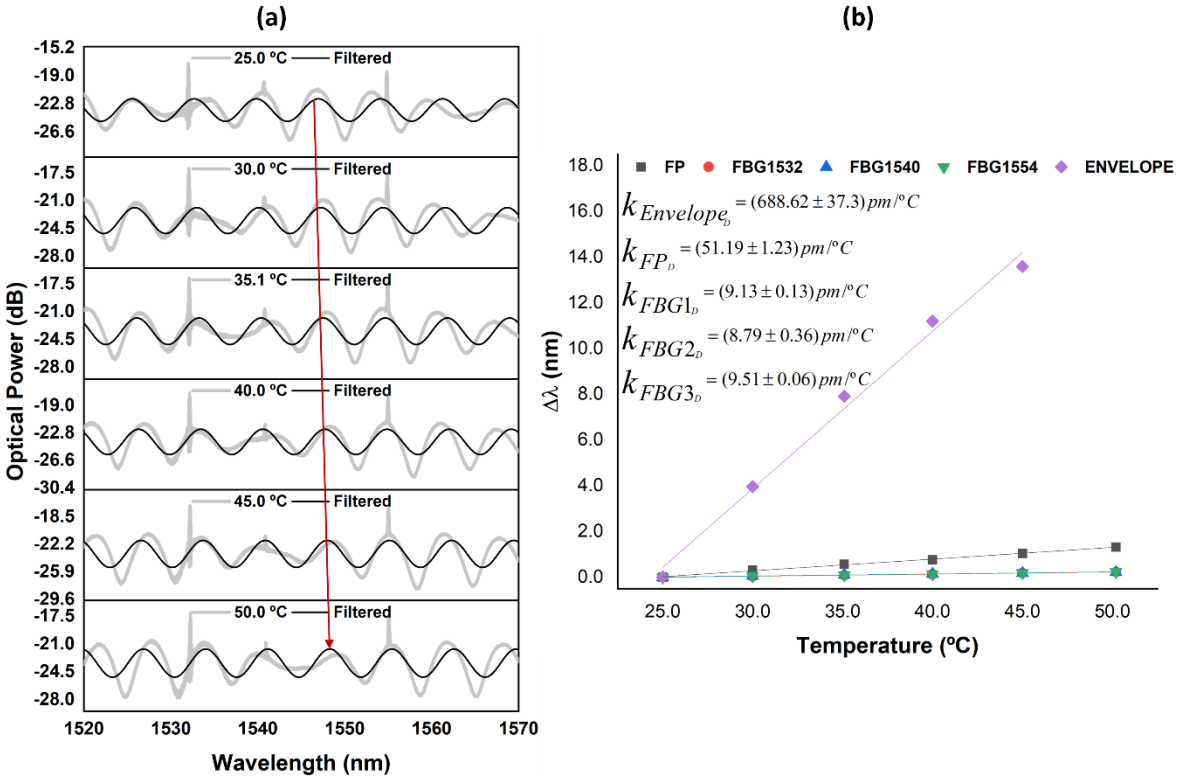

Figure 23 - Spectral response at each step and (b) linear fits of the hybrid sensor D for the temperature calibration.

Table 3 - Temperature sensitivities obtained for the calibrated hybrid sensors.

Sensitivity	Hybrid sensor B	Hybrid sensor C	Hybrid sensor D
k_{FBG_1} (pm/°C)	9.33 ± 0.79 R^2=0.9790	8.31 ± 0.24 R^2=0.9941	9.13 ± 0.13 R^2=0.9992
k_{FBG_2} (pm/°C)	10.31 ± 0.43 R^2=0.9949	8.14 ± 0.34 R^2=0.9882	8.79 ± 0.36 R^2=0.9932
k_{FBG_3} (pm/°C)	8.65 ± 0.23 R^2=0.9979	9.46 ± 0.42 R^2=0.9862	9.51 ± 0.06 R^2=0.9998
k_{FP} (pm/°C)	87.61 ± 8.17 R^2=0.9746	87.52 ± 3.40 R^2=0.9891	51.19 ± 1.23 R^2=0.9977
$k_{ENVELOPE}$ (nm/°C)	1.53 ± 0.23 R^2=0.9347	0.71± 0.02 R^2=0.9974	0.69 ± 0.04 R^2=0.9913

By analysing the data from Table 3, it is possible to apprehend that the FBGs present similar temperature sensitivity to the ones presented in the literature [19], therefore the slight bend caused by the liquid polymer's cavity weight did not influence the sensitivity of the closest FBG to the HCF section (FBG 1). Regarding the values achieved for FP_{dips} and the envelope, they were much higher, but with a coefficient of determination that resembles a non-linear behaviour. However, hybrid sensor B achieved a higher sensitivity than the ones reported in [10]-[12], [14], and [15]. With the increase in temperature, the liquid polymer's cavity expands and, for the envelope sensitivity to be greater than the FP_{dips}, it means that L_{C2} grew more towards the end face of the HCF than to the end face of the PS-SMF.

5.2 Hybrid sensors' pressure characterization

Similar for the temperature characterization analysis, in figures 24 (a), 25 (a), and 26 (a) are represented the full reflection spectrum of the hybrid sensor B, C, and D at each pressure calibration's step, respectively. The arrow in each graph represents the spectrum points used to obtain the pressure sensitivities for the FP, k_{FP}, and how the spectrum varies with the 1.0 bar intervals, however, calibration steps of 0.2 bar were used. In figures 24 (b), 25 (b), and 26 (b) are represented the corresponding sensitivities, with the summarized results presented in Table 4.

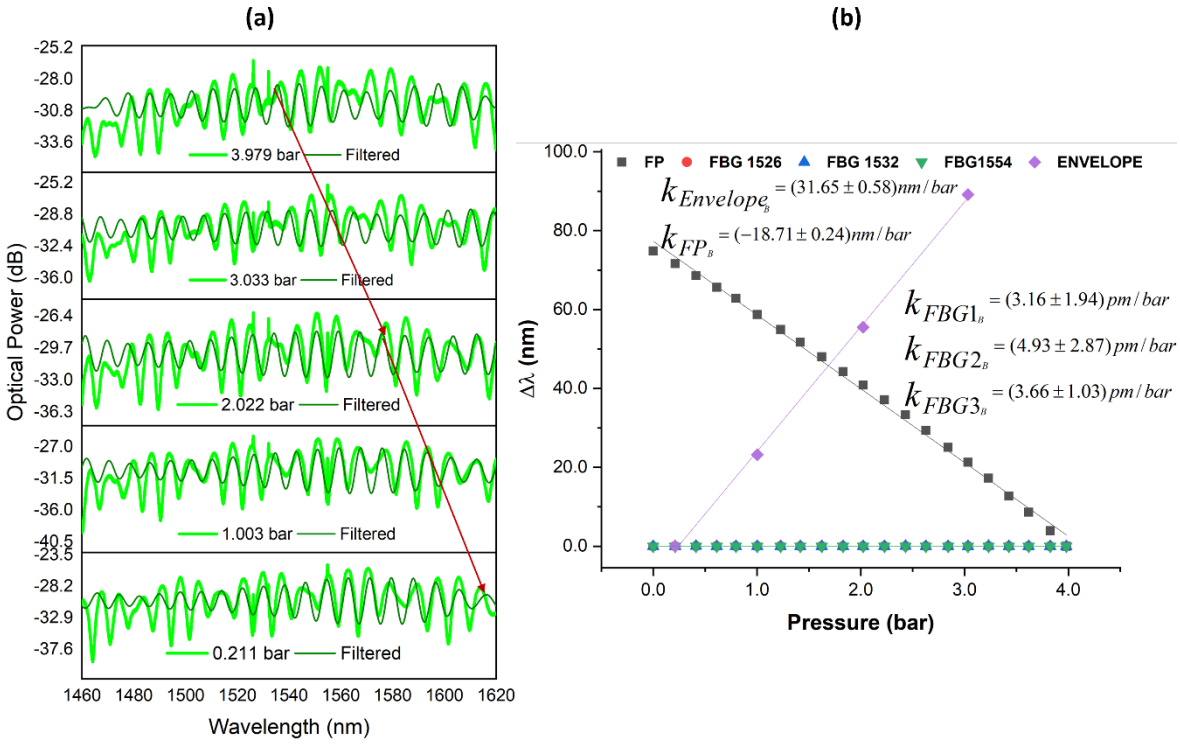

Figure 24 - (a) Spectral response at each step and (b) linear fits of the hybrid sensor B for the pressure calibration.

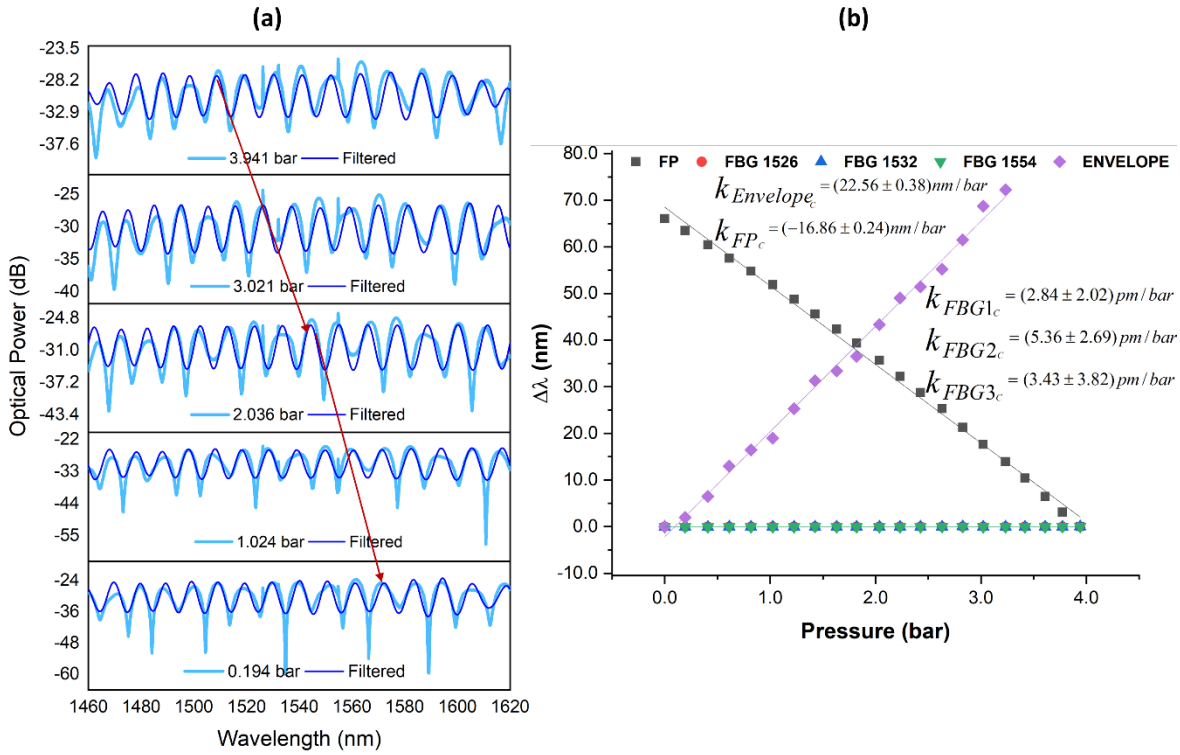

Figure 25 - Spectral response at each step and (b) linear fits of the hybrid sensor C for the pressure calibration.

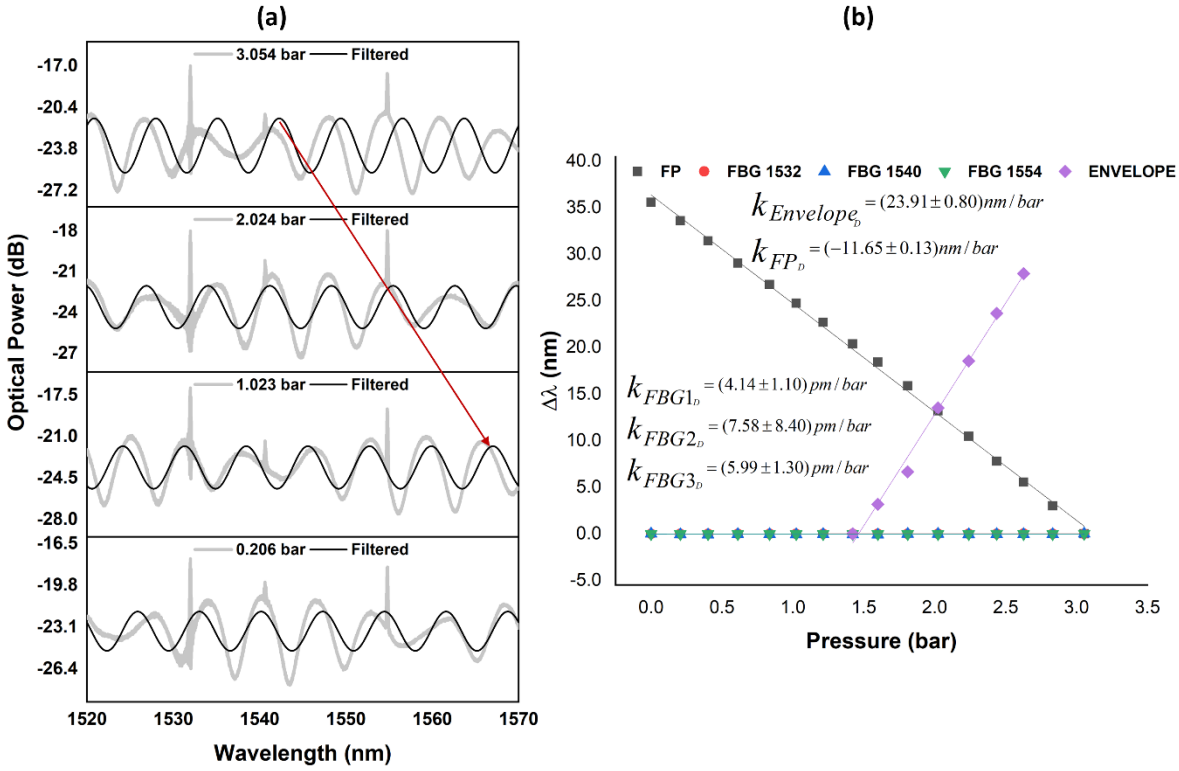

Figure 26 - (a) Spectral response at each step and (a) linear fits of the hybrid sensor D for the pressure calibration.

Table 4 - Pressure sensitivities obtained for the calibrated hybrid sensors.

Sensitivity	Hybrid sensor B	Hybrid sensor C	Hybrid sensor D
k_{FBG_1} (pm/bar)	3.16 ± 1.94 R^2=0.1231	2.84 ± 2.02 R^2=0.0939	4.14 ± 1.10 R^2=0.4923
k_{FBG_2} (pm/bar)	4.93 ± 2.87 R^2=0.1344	5.36 ± 2.69 R^2=0.1723	7.58 ± 8.40 R^2=0.0547
k_{FBG_3} (pm/bar)	3.66 ± 1.03 R^2=0.4009	3.43 ± 3.82 R^2=0.0408	5.99 ± 1.30 R^2=0.5810
k_{FP} (nm/bar)	-18.71 ± 0.24 R^2=0.9969	-16.86 ± 0.24 R^2=0.9961	-11.65 ± 0.13 R^2=0.9982
$k_{ENVELOPE}$ (nm/bar)	31.65 ± 0.58 R^2=0.9993	22.56 ± 0.38 R^2=0.9958	21.89 ± 0.80 R^2=0.9945

As the linear fit of the FBGs pressure calibration has a very low coefficient of determination, it is possible to conclude that, at this low-pressure range (0.0 to 4.0 bar), the FBGs are almost insensitive to pressure variations. So, on further calculations, it will be used a 0.3 pm/bar value, as described in [37]. The linear fit of the dips and envelope data generated a very good linearity, deriving from the +0.99 coefficient of determination. The highest sensitivity was, once more, achieved for the hybrid sensor B with 31.65 nm/bar, and this value is higher than all the works

presented in Section 1.1, and, to the best of our knowledge, greater than any other. The symmetrical sensitivities demonstrated from the FP_{dips} and the envelope data can be explained through the cavities length evolution with decreasing pressure. As pressure decreases, the liquid polymer's cavity expands at a rate that L_{C2} is decreasing in length and L_{C1} is increasing.

5.3 Temperature and pressure tracking during lithium-ion batteries' operation

The temperature and pressure variations during both galvanostatic cyclic tests are shown in Figure 27, at an ambient temperature of 25.0 °C, and in Figure 28, at an ambient temperature of 40.0 °C, which were acquired by using the sensitivity matrix presented in equations 31 to 33, containing the sensitivities of hybrid sensor D, and by introducing the wavelength shifts of the spectrum dips and internal FBGs:

$$\text{Hybrid sensor D (positive)}: \begin{bmatrix}\Delta P\\ \Delta T\end{bmatrix} = \frac{1}{M_{D1}}\begin{bmatrix}0.05119 & -0.00913\\ -11.65 & 0.0003\end{bmatrix}\begin{bmatrix}\Delta\lambda_{FBG1}\\ \Delta\lambda_{FP}\end{bmatrix}, \quad (31)$$

$$\text{Hybrid sensor D (middle)}: \begin{bmatrix}\Delta P\\ \Delta T\end{bmatrix} = \frac{1}{M_{D2}}\begin{bmatrix}0.05119 & -0.00879\\ -11.65 & 0.0003\end{bmatrix}\begin{bmatrix}\Delta\lambda_{FBG3}\\ \Delta\lambda_{FP}\end{bmatrix}, \quad (32)$$

$$\text{Hybrid sensor D (negative)}: \begin{bmatrix}\Delta P\\ \Delta T\end{bmatrix} = \frac{1}{M_{D3}}\begin{bmatrix}0.05119 & -0.00951\\ -11.65 & 0.0003\end{bmatrix}\begin{bmatrix}\Delta\lambda_{FBG3}\\ \Delta\lambda_{FP}\end{bmatrix}, \quad (33)$$

with $M_{D1} = -0.106$, $M_{D2} = -0.102$, and $M_{D3} = -0.111$. Although the sensitivity was higher for the envelope data, the sensitivity matrix contains the FP_{dips} sensitivities because, when testing with the envelope one, the spectral window of 1460 to 1620 nm was not enough to analyse the spectral shifts occurring during the galvanostatic cyclic tests. From a general perspective of the temperature evolution, there are several conclusions that are possible to take: the temperature signals detected by the internal sensors mainly follows the external FBGs data, but with a more amplified expression, which means that some internal thermal events are not tracked by the external sensors; internally, the battery is more prone to temperature variations than externally, and, in the middle section of the battery, occurred the highest temperature shifts, reaching more than +4.0 °C at several charging stages (Figure 27 and 28). When the battery was charging, the temperature increased and the same phenomenon occurred during the discharging step, but with a lower shift, except at the end of it, where sensors detected a spike accompanied with a rapid decrease in voltage and battery's capacity (Figure 29). During the resting step, the battery was able to stabilize its temperature, thus decreasing.

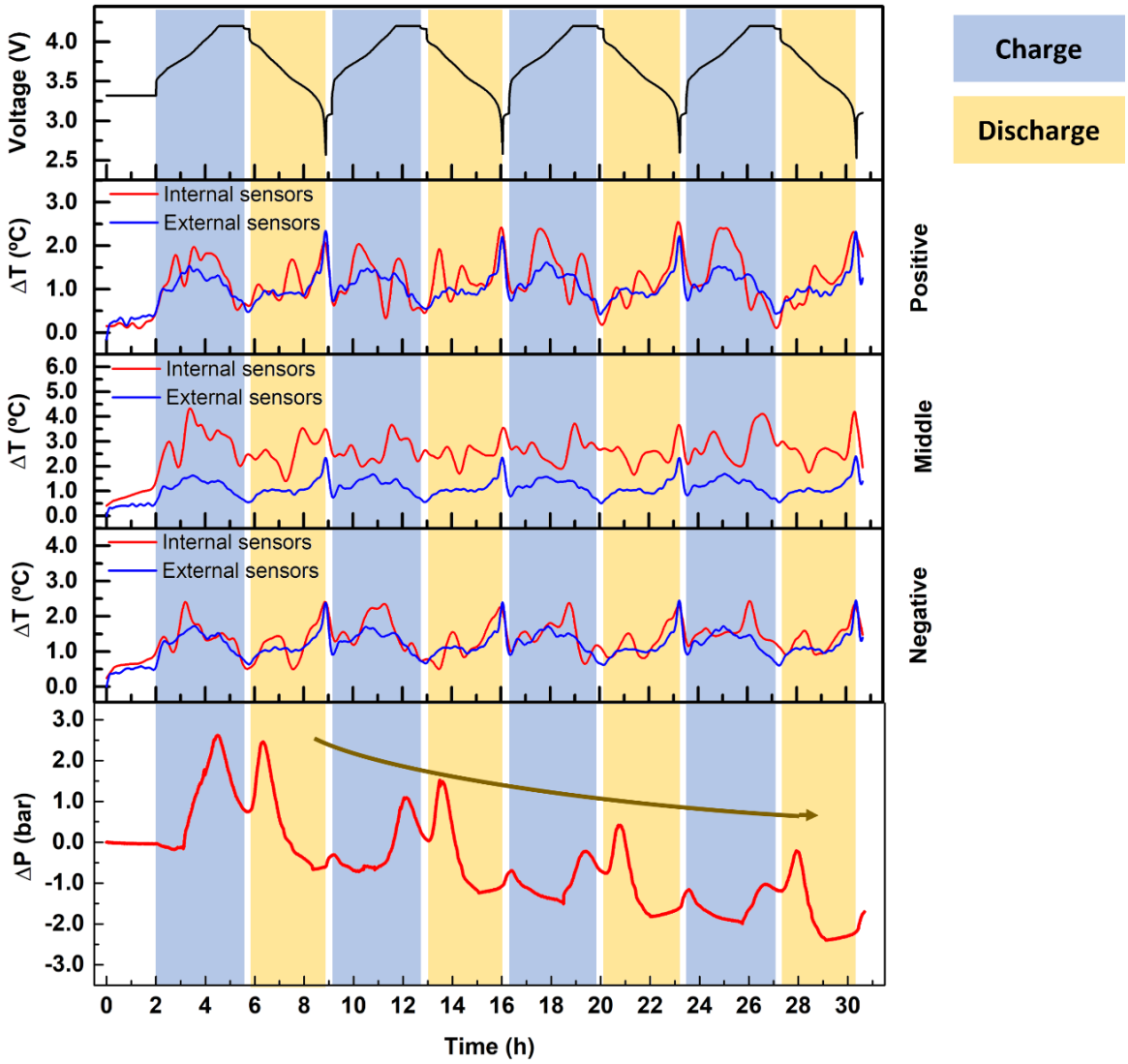

Figure 27 - Temperature and pressure variation evolution for the galvanostatic cyclic test performed at 25.0ºC, with each charge (blue area) and discharge steps (yellow area), and the resting steps (white areas) represented. The first layer refers to the voltage profile, while the second, third and fourth are related to the positive terminal, middle of the battery, and negative terminal's temperature shifts, respectively (internal variation - red; external variation - blue). The fifth layer demonstrates the pressure variation inside the battery (red).

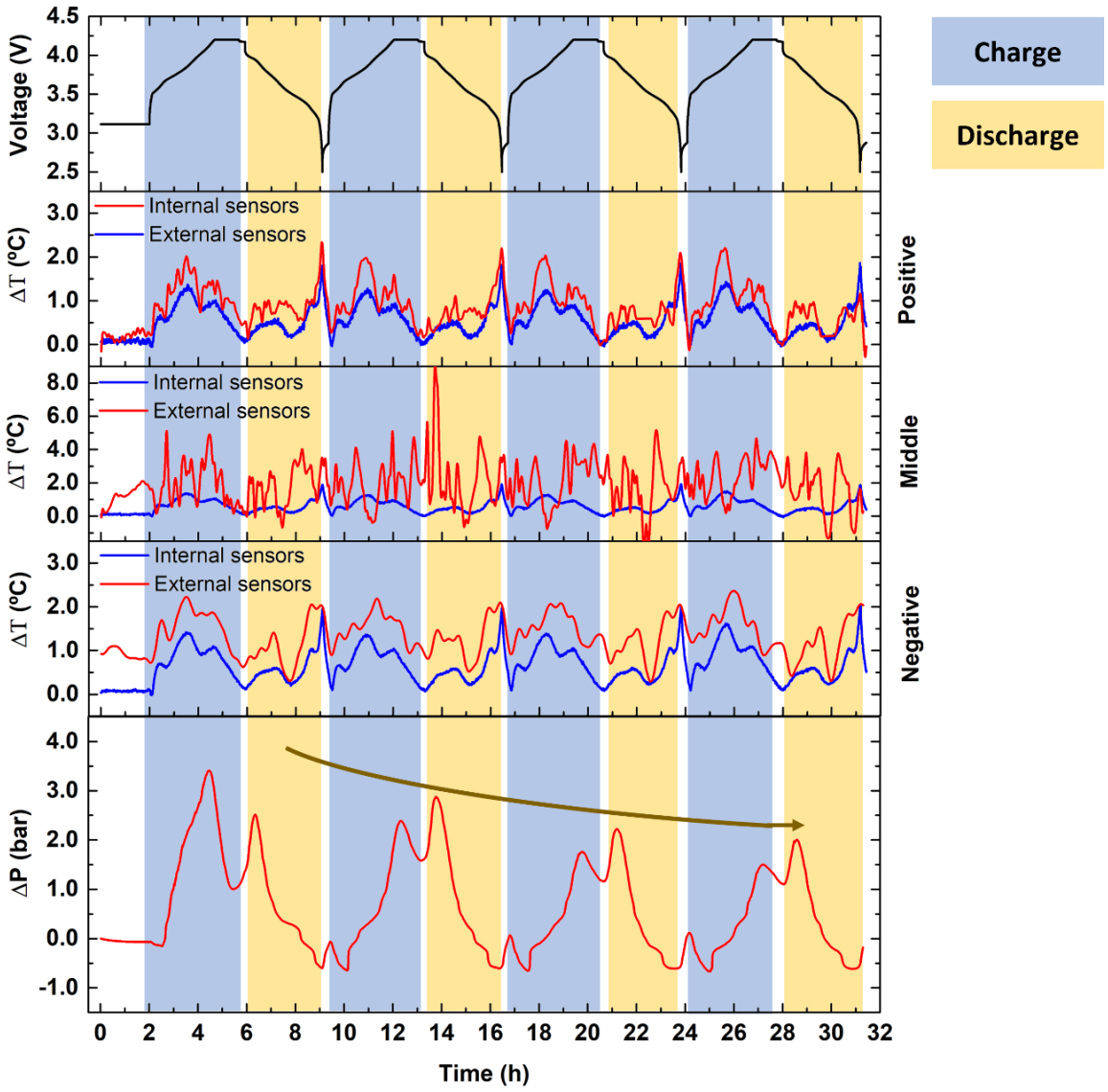

Figure 28 - Temperature and pressure variation evolution for the galvanostatic cyclic test performed at 40.0ºC, with each charge (blue area) and discharge steps (yellow area), and the resting steps (white areas) represented. The first layer refers to the voltage profile, while the second, third and fourth are related to the positive terminal, middle of the battery, and negative terminal's temperature shifts, respectively (internal variation - red; external variation - blue). The fifth layer demonstrates the pressure variation inside the battery (red).

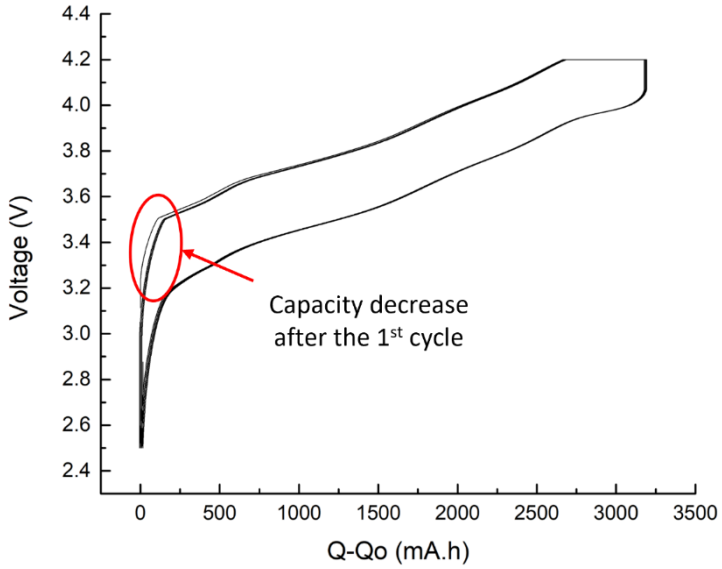

Figure 29 - Voltage evolution with the battery's capacity during the galvanostatic cyclic test at 25.0 ºC. At 40.0 ºC, it was observed a similar evolution.

The positive and negative terminals of the battery detected almost the same battery thermal variation, but, with a more detailed analysis of the first charge step, Figure 30 (a), it appears that a thermal flux is flowing from the negative terminal towards the positive terminal, which could be a sign of the internal electrochemical flows promoted by the Li^+ movement during the battery's operation. A symmetrical behaviour occurs in the first discharge step, Figure 30 (b), where a thermal flux presents itself, originating in the positive terminal and flowing towards the negative one. The middle profile shows a very similar progression than the one presented in the literature, however for a different battery's chemistry [22], where four peaks are presented in the charge step (*i*, *ii*, *iii*, *iv*) and two peaks at the discharge step (*v* and *iv*). The *ii* peak disappears on the successive cycles, which can be associated with the greater pressure increase in the first charge step, Figure 31, meaning that it was more gas generated, leading to the creation of the SEI layer [22]. Regarding the initial rest period, the external FBGs detected a constant temperature, but internally, it showed some evolution, possibly meaning that the internal temperature was not stabilized even after two hours.

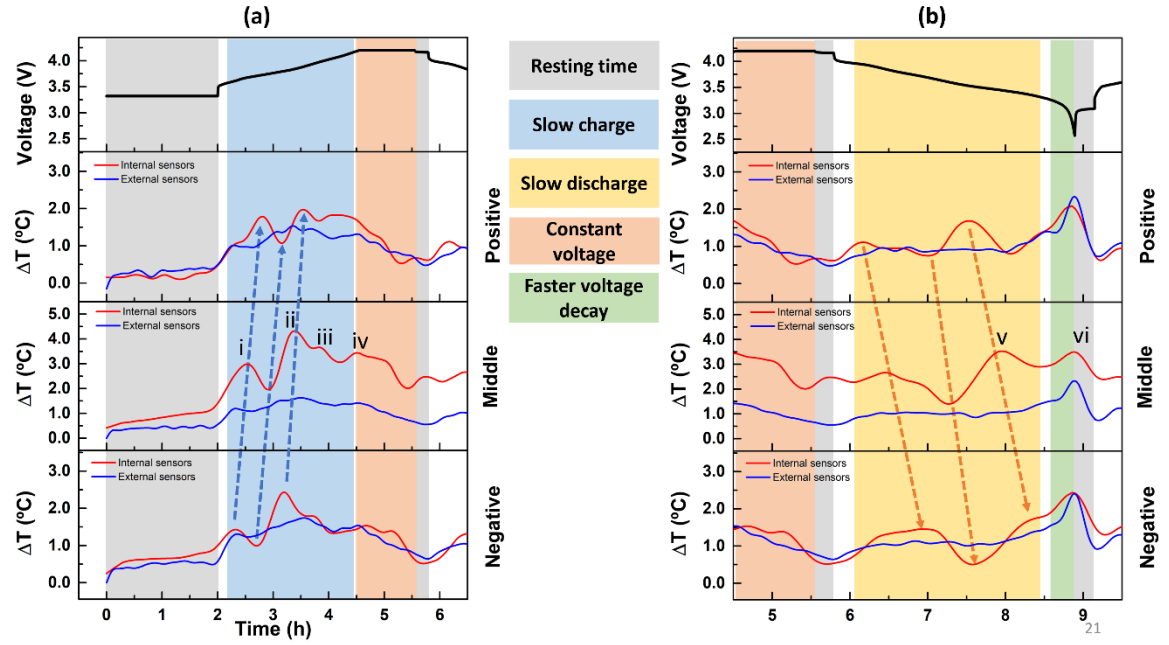

Figure 30 - Amplification of the temperature variation profile during the first cycle at the (a) charge and (b) discharge step. i to iv represent six temperature peaks for the middle section, in accordance with [22].

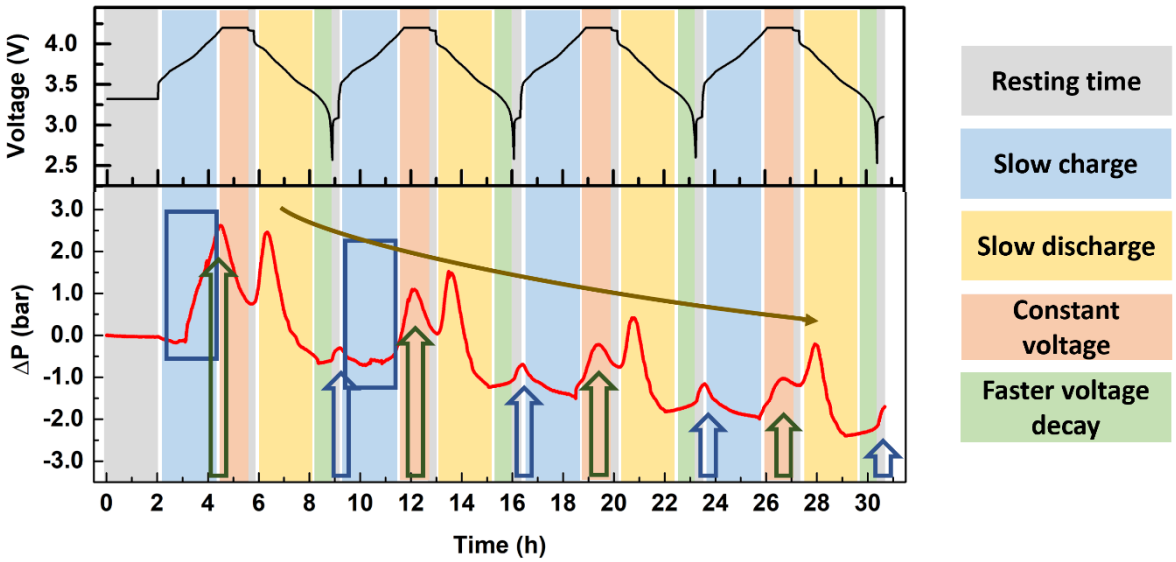

Figure 31 - Pressure variation profile inside for the galvanostatic cyclic test at 25.0 ºC. The blue squares represent the difference in the pressure evolution from the first charge step to the following ones, while the green arrows represent the pressure decrease over time, and the blue arrows the pressure increase at the end of each cycle.

At room temperature of 40.0 °C, only at the middle region was detected a major increase in temperature (± 2.0 °C) in the rest period, Figure 28. At the start of each charge step, the external temperature has risen with almost the same progression as internally, and the thermal flux visible at 25.0 °C is no longer detectable. At the constant voltage step, the temperature has decreased over its duration. With the beginning of the discharge step, the temperature increased slightly. Then, at the end of the stage, with the rapid voltage decay and loss of battery capacity, a major temperature spike occurred, with it being constant throughout all discharging steps' ending. The

external temperature variation detected by all the external FBGs, in these cases, perfectly matched the internal ones.

Regarding pressure variation, its evolution was very similar during all galvanostatic cycles, considering both ambient temperatures, although the graphics presented in Figure 27 and Figure 28 were made assuming that the pressure sensed by the hybrid sensor, near the positive terminal, was the same as in another section of the battery. Regardless, it is possible to observe that, with each repeated cycle, the pressure variation continuously decreases and, at 25.0 °C, to lower pressure values than its starting one, Figure 28 and 31. Only on the first cycle occurred a greater pressure variation on the charge step (~2.6 bar at 25.0 °C, and ~3.4 bar at 40.0 °C) than in the discharge step (~2.50 bar at both temperatures), which can be related to the smaller capacity difference at the same voltage level of the successive cycles, derived by the increase in gas generation, as seen previously. At an external temperature of 40.0 °C, the charge step pressure increase presented a ~0.90 bar decline throughout the three cycles, the same as at the discharge step. On the other hand, at 25.0 °C, across the last three cycles, the pressure peaks shifted from ~-2.0 bar to ~-1.0 bar and ~-0.4 bar, respectively for the charge step and the discharge step pressure's peak. The pressure remains stable during the initial rest and only increases after it reaches around 3.77 V, which is indicative of the gas generation moment. At constant voltage, the pressure decreases and stabilizes during the 15-minute rest, just like in the beginning. With the discharge step, it increases until the battery reaches ~3.90 V. After this, the pressure lowers until it stabilizes again at the start of the rapid voltage decay.

Chapter 6- Summary and future work

In this work, it was proposed and successfully developed an innovative hybrid sensing design that can discriminate simultaneously internal pressure and temperature variations in an 18650 LiB, commercially used in battery packs to power electric vehicles, for the first time. It was shown the steps taken to reach the final optimal characteristics of the hybrid sensor and how it can translate the wavelength shifts of the FBGs and the FPI to pressure and temperature.

Although several procedures from the sensors' manufacturing were not performed in the most precise way, it can be acknowledged that, with some technical upgrades, like some sort of magnifying glass to help cleave the HCF tube and its deposition in the liquid polymer's droplet, this sensor can be highly reproductible. Several hybrid sensors (A to D) were developed and fully characterized to temperature and pressure parameters.

The highest temperature sensitivity was achieved for the hybrid sensor B, with 1.53 nm/°C (through the envelope), which corresponds to the lowest theoretical liquid polymer's cavity length (23.63 µm). With the increase of temperature, the viscosity of the UV-glue can decrease and, for lower $\mathrm{L_{C2}}$, it can deform more. Regarding the pressure sensitivity, the highest value was obtained for the hybrid sensor B, with 31.65 nm/bar (through the envelope), but this does not translate to the lowest $\mathrm{L_{C2}}$ length, which is inherent to the hybrid sensor D. With lower liquid polymer's cavity length, less quantity of material is in fact in it, therefore, the cavity is more susceptible to pressure variations, which should translate to a higher sensitivity. In this case, the higher sensitivity was due to the lower proportion of $\mathrm{L_{C2}}/\mathrm{L_{C1}}$ (from the theoretical values in Table 2).

The temperature and pressure variation data, through the matrixial method, provides interesting information about the battery's behaviour, and the differences between normal (25.0 °C) and abnormal (40.0 °C) operating conditions. The positive and negative terminals temperature variations were very similar in both tests; on the other hand, the pressure variation was higher at 40.0 °C than at 25.0 °C. The pressure profile detected in the first charge cycle was the same for both tests and was due to the same reason: increase in gas generation. The temperature variation detected in the middle of the battery, mainly determined by the FBG 1540, is more unstable driven from the multiple electrochemical events occurring and, since it is in the middle of the battery, it is affected by the thermal variations of the battery's extremities. In this way, it should be highlighted that the hybrid sensor developed tracked internal thermal and pressure events that, by using just the external sensors, are completely imperceptible.

In sum, this work presented a new and more sensitive way of simultaneous pressure and temperature data discrimination in a specific application, from two different sensing structures and can shed some light into the potential of the hybrid sensors development based on FPI coupled with FBG sensors.

As this work is based on an innovative hybrid sensor, there are many experiments that are possible to set up to understand more clearly the potential of this sensor in performing internal measurements in LiBs.

A very crucial property of any sensor is its long-term stability. As the electric automotive industry develops electric vehicles with higher autonomy and battery life-cycle endurance, the

sensors must also accompany this growth and output, as reliably as possible, the accurate behaviour of LiBs, such as voltage, temperature, state-of-charge, among others. As seen previously, there are several stress situations that can trigger the release of toxic gases. Therefore, a long-term test must be conducted on this hybrid sensor, with the liquid polymer's cavity made of cured NOA 85, to assess if any corrosion process is occurring in the fiber optic itself and in the UV-photosensitive polymer, both of which can deteriorate the accurate discrimination of pressure and temperature variations.

As the developed hybrid sensors can only be manufactured on the fiber's tip, and were localized near the positive terminal of the batteries, and if all pressure variations detected occurs with the same profile in all battery's location, a new configuration of the hybrid sensors' locations for internal measurements could be tested, where the hybrid sensors could be jointed in such a way that each set of FBG and IFPI can perform direct internal measurements in the negative and positive terminals, and in the middle of the battery, giving a much more accurate readings of the processes occurring inside the battery, and to understand if the pressure behaves differently inside the batteries. Inserting the proposed sensor in different types of LiBs, like pouch cells and prismatic, can also be an interesting challenge and very useful to perform a comparative study on different thermal and pressure variations during their charging and discharging steps.

Given the promising results acquired from the galvanostatic cyclic tests at 25.0 °C, normal conditions, and 40.0 °C, abnormal conditions, it can be performed additional tests at higher (60.0 °C) and lower temperatures (0.0 °C), to simulate even harsher working conditions for the LiBs.

References

[1] F. Hoeft, "Internal combustion engine to electric vehicle retrofitting: Potential customer's needs, public perception and business model implications," *Transp Res Interdiscip Perspect*, vol. 9, Mar. 2021, doi: 10.1016/j.trip.2021.100330.

[2] L. Komsiyska *et al.*, "Critical review of intelligent battery systems: Challenges, implementation, and potential for electric vehicles," *Energies (Basel)*, vol. 14, no. 18, Sep. 2021, doi: 10.3390/en14185989.

[3] Y. Chen *et al.*, "A review of lithium-ion battery safety concerns: The issues, strategies, and testing standards," *Journal of Energy Chemistry*, vol. 59. Elsevier B.V., pp. 83–99, Aug. 01, 2021. doi: 10.1016/j.jechem.2020.10.017.

[4] L. Lu, X. Han, J. Li, J. Hua, and M. Ouyang, "A review on the key issues for lithium-ion battery management in electric vehicles," *Journal of Power Sources*, vol. 226. pp. 272–288, Mar. 15, 2013. doi: 10.1016/j.jpowsour.2012.10.060.

[5] H. Zhang, R. Lu, C. Zhu, and Y. Zhao, "On-line Measurement of Internal Resistance of Lithium Ion Battery for EV and Its Application Research," *International Journal of u- and e-Service, Science and Technology*, vol. 7, no. 4, pp. 301–310, Aug. 2014, doi: 10.14257/ijunesst.2014.7.4.27.

[6] Y. D. Su, Y. Preger, H. Burroughs, C. Sun, and P. R. Ohodnicki, "Fiber optic sensing technologies for battery management systems and energy storage applications," *Sensors (Switzerland)*, vol. 21, no. 4. MDPI AG, pp. 1–36, Feb. 02, 2021. doi: 10.3390/s21041397.

[7] D.-W. Duan, Y. Rao, Y.-S. Hou, and T. Zhu, "Microbubble based fiber-optic Fabry–Perot interferometer formed by fusion splicing single-mode fibers for strain measurement," *Appl Opt*, vol. 51, no. 8, pp. 1033–1036, Mar. 2012, doi: 10.1364/AO.51.001033.

[8] B. Sun *et al.*, "Simultaneous measurement of pressure and temperature by employing Fabry-Perot interferometer based on pendant polymer droplet," *Opt Express*, vol. 23, no. 3, p. 1906, Feb. 2015, doi: 10.1364/oe.23.001906.

[9] D. W. Kim, F. Shen, X. Chen, and A. Wang, "Simultaneous measurement of refractive index and temperature based on a reflection-mode long-period grating and an intrinsic Fabry–Perot

interferometer sensor," *Opt Lett*, vol. 30, no. 22, pp. 3000–3002, Nov. 2005, doi: 10.1364/OL.30.003000.
[10] H. Gao, D. Xu, Y. Ye, Y. Zhang, J. Shen, and C. Li, "Fiber-tip polymer filled probe for high-sensitivity temperature sensing and polymer refractometers," *Opt Express*, vol. 30, no. 5, p. 8104, Feb. 2022, doi: 10.1364/oe.449852.
[11] B. Xu, Y. M. Liu, D. N. Wang, and J. Q. Li, "Fiber Fabry-Pérot Interferometer for Measurement of Gas Pressure and Temperature," *Journal of Lightwave Technology*, vol. 34, no. 21, pp. 4920–4925, Nov. 2016, doi: 10.1109/JLT.2016.2598573.
[12] W. P. Chen, D. N. Wang, B. Xu, C. L. Zhao, and H. F. Chen, "Multimode fiber tip Fabry-Perot cavity for highly sensitive pressure measurement," *Sci Rep*, vol. 7, no. 1, Dec. 2017, doi: 10.1038/s41598-017-00300-x.
[13] Z. Zhang *et al.*, "High-Sensitivity Gas-Pressure Sensor Based on Fiber-Tip PVC Diaphragm Fabry-Pérot Interferometer," *Journal of Lightwave Technology*, vol. 35, no. 18, pp. 4067–4071, Sep. 2017, doi: 10.1109/JLT.2017.2710210.
[14] Y. Liu *et al.*, "Miniature fiber-optic tip pressure sensor assembled by hydroxide catalysis bonding technology," *Opt Express*, vol. 28, no. 2, p. 948, Jan. 2020, doi: 10.1364/oe.380589.
[15] S. Zhang *et al.*, "An optical fiber pressure sensor with ultra-thin epoxy film and high sensitivity characteristics based on blowing bubble method," *IEEE Photonics J*, vol. 13, no. 1, Feb. 2021, doi: 10.1109/JPHOT.2021.3055872.
[16] C. Lang, Y. Liu, Y. Liao, J. Li, and S. Qu, "Ultra-Sensitive Fiber-Optic Temperature Sensor Consisting of Cascaded Liquid-Air Cavities Based on Vernier Effect," *IEEE Sens J*, vol. 20, no. 10, pp. 5286–5291, May 2020, doi: 10.1109/JSEN.2020.2970431.
[17] G. Yang, C. Leitão, Y. Li, J. Pinto, and X. Jiang, "Real-time temperature measurement with fiber Bragg sensors in lithium batteries for safety usage," *Measurement (Lond)*, vol. 46, no. 9, pp. 3166–3172, 2013, doi: 10.1016/j.measurement.2013.05.027.
[18] S. Novais *et al.*, "Internal and external temperature monitoring of a li-ion battery with fiber bragg grating sensors," *Sensors (Switzerland)*, vol. 16, no. 9, Sep. 2016, doi: 10.3390/s16091394.
[19] M. Nascimento, M. S. Ferreira, and J. L. Pinto, "Real time thermal monitoring of lithium batteries with fiber sensors and thermocouples: A comparative study," *Measurement (Lond)*, vol. 111, pp. 260–263, Dec. 2017, doi: 10.1016/j.measurement.2017.07.049.
[20] J. Fleming, T. Amietszajew, E. McTurk, D. Greenwood, and R. Bhagat, "Development and evaluation of in-situ instrumentation for cylindrical Li-ion cells using fibre optic sensors," *HardwareX*, vol. 3, pp. 100–109, Apr. 2018, doi: 10.1016/j.ohx.2018.04.001.
[21] K. M. Alcock, M. Grammel, Á. González-Vila, L. Binetti, K. Goh, and L. S. M. Alwis, "An accessible method of embedding fibre optic sensors on lithium-ion battery surface for in-situ thermal monitoring," *Sens Actuators A Phys*, vol. 332, Dec. 2021, doi: 10.1016/j.sna.2021.113061.
[22] J. Huang *et al.*, "Operando decoding of chemical and thermal events in commercial Na(Li)-ion cells via optical sensors," *Nat Energy*, vol. 5, no. 9, pp. 674–683, Sep. 2020, doi: 10.1038/s41560-020-0665-y.
[23] M. Nascimento *et al.*, "Internal strain and temperature discrimination with optical fiber hybrid sensors in Li-ion batteries," *J Power Sources*, vol. 410–411, pp. 1–9, Jan. 2019, doi: 10.1016/j.jpowsour.2018.10.096.
[24] Y. Liu *et al.*, "Fabrication of dual-parameter fiber-optic sensor by cascading FBG with FPI for simultaneous measurement of temperature and gas pressure," *Opt Commun*, vol. 443, pp. 166–171, Jul. 2019, doi: 10.1016/j.optcom.2019.03.034.
[25] L. Kong, C. Li, J. Jiang, and M. G. Pecht, "Li-ion battery fire hazards and safety strategies," *Energies (Basel)*, vol. 11, no. 9, 2018, doi: 10.3390/en11092191.
[26] Y. Liu, R. Zhang, J. Wang, and Y. Wang, "iScience Perspective Current and future lithium-ion battery manufacturing," *iScience*, vol. 24, p. 102332, 2021, doi: 10.1016/j.isci.
[27] J. Xie and Y. C. Lu, "A retrospective on lithium-ion batteries," *Nature Communications*, vol. 11, no. 1. Nature Research, Dec. 01, 2020. doi: 10.1038/s41467-020-16259-9.
[28] X. Y. Yao and M. G. Pecht, "Tab design and failures in cylindrical li-ion batteries," *IEEE Access*, vol. 7, pp. 24082–24095, 2019, doi: 10.1109/ACCESS.2019.2899793.
[29] "PRODUCT SPECIFICATION - Rechargeable Lithium Ion Battery INR18650 MH1 3200mAh." [Online]. Available: http://www.lgchem.com

[30] X. Y. Yao, S. Saxena, L. Su, and M. G. Pecht, “The Explosive Nature of Tab Burrs in Li-Ion Batteries,” *IEEE Access*, vol. 7, pp. 45978–45982, 2019, doi: 10.1109/ACCESS.2019.2909018.
[31] D. Deng, “Li-ion batteries: Basics, progress, and challenges,” *Energy Science and Engineering*, vol. 3, no. 5. John Wiley and Sons Ltd, pp. 385–418, Sep. 01, 2015. doi: 10.1002/ese3.95.
[32] T. R. Jow, S. A. Delp, J. L. Allen, J.-P. Jones, and M. C. Smart, “ Factors Limiting Li + Charge Transfer Kinetics in Li-Ion Batteries ,” *J Electrochem Soc*, vol. 165, no. 2, pp. A361–A367, 2018, doi: 10.1149/2.1221802jes.
[33] M. Kaliaperumal *et al.*, “Cause and mitigation of lithium-ion battery failure—a review,” *Materials*, vol. 14, no. 19, Oct. 2021, doi: 10.3390/ma14195676.
[34] M. Nascimento, M. S. Ferreira, and J. L. Pinto, “Simultaneous sensing of temperature and bi-directional strain in a prismatic li-ion battery,” *Batteries*, vol. 4, no. 2, Jun. 2018, doi: 10.3390/batteries4020023.
[35] S. J. Petuchowski, T. G. Giallorenzi, and S. K. Sheem, “A Sensitive Fiber-optic Fabry-Perot Interferometer,” 1981.
[36] M. Rajibul Islam, M. Mahmood Ali, M. H. Lai, K. S. Lim, and H. Ahmad, “Chronology of fabry-perot interferometer fiber-optic sensors and their applications: A review,” *Sensors (Switzerland)*, vol. 14, no. 4. Molecular Diversity Preservation International, pp. 7451–7488, Apr. 24, 2014. doi: 10.3390/s140407451.
[37] M. G. Xu, L. Reekie, Y. T. Chow, and J. P. Dakin, “Optical in-fibre grating high pressure sensor,” *Electron Lett*, vol. 29, no. 4, pp. 398–399, 1993.
[38] M. Born and E. Wolf, *Principles of Optics*. Pergamon , 1980.
[39] A. D. Gomes *et al.*, “Optical harmonic vernier effect: A new tool for high performance interferometric fibre sensors,” *Sensors (Switzerland)*, vol. 19, no. 24, Dec. 2019, doi: 10.3390/s19245431.
[40] A. M. Aizzuddin, Z. M. Hafizi, L. v. Kee, E. Vorathin, and K. S. Lim, “Development of Fibre Bragg grating (FBG) dynamic pressure transducer with diminutive voltage inconsistency,” in *IOP Conference Series: Materials Science and Engineering*, Nov. 2017, vol. 257, no. 1. doi: 10.1088/1757-899X/257/1/012080.
[41] N. T. Anh *et al.*, “Determination of Wavelength Shift of Fiber Bragg Grating Sensors by Tunable Single-mode Diode Laser,” *Communications in Physics*, vol. 23, no. 1, p. 67, Apr. 2013, doi: 10.15625/0868-3166/23/1/2613.
[42] S. Zhang, Y. Mei, T. Xia, Z. Cao, Z. Liu, and Z. Li, “Simultaneous Measurement of Temperature and Pressure Based on Fabry-Perot Interferometry for Marine Monitoring,” *Sensors*, vol. 22, no. 13, Jul. 2022, doi: 10.3390/s22134979.
[43] O. Frazão and J. L. Santos, “Simultaneous measurement of strain and temperature using a Bragg grating structure written in germanosilicate fibres,” *Journal of Optics A: Pure and Applied Optics*, vol. 6, no. 6, pp. 553–556, Jun. 2004, doi: 10.1088/1464-4258/6/6/010.
[44] J. R. Belt, D. M. Bernardi, and V. Utgikar, “Development and Use of a Lithium-Metal Reference Electrode in Aging Studies of Lithium-Ion Batteries,” *J Electrochem Soc*, vol. 161, no. 6, pp. A1116–A1126, May 2014, doi: 10.1149/2.062406jes.
[45] T. A. Vincent, B. Gulsoy, J. E. H. Sansom, and J. Marco, “In-situ instrumentation of cells and power line communication data acquisition towards smart cell development,” *J Energy Storage*, vol. 50, p. 104218, Jun. 2022, doi: 10.1016/j.est.2022.104218.